

AD-A256 782



12

The Pennsylvania State University
APPLIED RESEARCH LABORATORY
P.O. Box 30
State College, PA 16804

DTIC
ELECTE
OCT 15 1992
S C D

NONLINEAR FINITE ELEMENT ANALYSIS OF
METALS AND METAL MATRIX COMPOSITES:
A LOCAL-GLOBAL INVESTIGATION

by

M. B. House, R. B. Bhagat

Technical Report No. TR 92-01
October 1992

Supported by:
Space and Naval Warfare Systems Command

L.R. Hettche, Director
Applied Research Laboratory

Approved for public release; distribution unlimited

92 10 14 050

39/007

92-27100



105pg

REPORT DOCUMENTATION PAGE

Form Approved
OAS No. 0704-0188

Public reporting burden for this collection of information is estimated to average 1 hour per response, including the time for reviewing instructions, searching existing data sources, gathering and maintaining the data needed, and completing and reviewing the collection of information. Send comments regarding this burden estimate or any other aspect of this collection of information, including suggestions for reducing this burden, to Washington Headquarters Service, Directorate for Information Operations and Reports, 1215 Jefferson Davis Highway, Suite 1204, Arlington, VA 22202-4302, and to the Office of Management and Budget, Paperwork Reduction Project (0704-0188), Washington, DC 20503.

1. AGENCY USE ONLY (Leave blank)		2. REPORT DATE October 1992		3. REPORT TYPE AND DATES COVERED	
4. TITLE AND SUBTITLE Nonlinear Finite Element Analysis of Metals and Metal Matrix Composites: A Local-Global Investigation				5. FUNDING NUMBERS	
6. AUTHOR(S) M. B. House, R. B. Bhagat					
7. PERFORMING ORGANIZATION NAME(S) AND ADDRESS(ES) The Applied Research Laboratory P.O. Box 30 State College, PA 16804				8. PERFORMING ORGANIZATION REPORT NUMBER TR-92-01	
9. SPONSORING/MONITORING AGENCY NAME(S) AND ADDRESS(ES) Space and Naval Warfare Systems Command Department of the Navy Washington, DC 20363-5000				10. SPONSORING/MONITORING AGENCY REPORT NUMBER N00039-88-C-0051	
11. SUPPLEMENTARY NOTES					
12a. DISTRIBUTION / AVAILABILITY STATEMENT Approved for Public Release. Distribution Unlimited.				12b. DISTRIBUTION CODE	
13. ABSTRACT (Maximum 200 words) A computational investigation of the fracture mechanics of metals and metal matrix composites has been carried out. The ductile fracture of structural alloys was analyzed through a two dimensional non-linear finite element approach, while the mechanics of load transfer in silicon carbide (SCS-6) fiber reinforced titanium alloy (Ti-15V-3Cr-3Al-3Sn) were studied using a local-global finite element analysis procedure. The computed values of the J -Integral for compact tension specimens of steel and aluminum alloys ($0.533 \leq a/W \leq 0.884$) remain path independent up to a certain load which is attributed to crack initiation, and then diverge. There is a unique signature of the strain energy density (dW/dV) ahead of the crack in the 0° direction: the strain energy first decreases, reaches a minimum and then increases with increasing distance from the crack tip. The minimum strain energy shows a unique dependence on the applied load. This leads to the prediction of the fracture loads for the cracked specimens. A novel coordinate system rotation was employed in extracting the boundary conditions from the two-dimensional global model to the three-dimensional local model for the local-global finite element analysis of the unidirectional composite.					
14. SUBJECT TERMS nonlinear, finite element, metal matrix, composites, metals, ductile fracture, alloys, silicon carbide, titanium, compact tension, steel, aluminum, cracks, strain energy				15. NUMBER OF PAGES 92	
				16. PRICE CODE	
17. SECURITY CLASSIFICATION OF REPORT UNCLASSIFIED	18. SECURITY CLASSIFICATION OF THIS PAGE UNCLASSIFIED	19. SECURITY CLASSIFICATION OF ABSTRACT UNCLASSIFIED	20. LIMITATION OF ABSTRACT		

ABSTRACT

A computational investigation of the fracture mechanics of metals and metal matrix composites has been carried out. The ductile fracture of structural alloys was analyzed through a two dimensional non-linear finite element approach, while the mechanics of load transfer in silicon carbide (SCS-6) fiber reinforced titanium alloy (Ti-15V-3Cr-3Al-3Sn) were studied using a local-global finite element analysis procedure.

The computed values of the J -Integral for compact tension specimens of steel and aluminum alloys ($0.533 \leq a/W \leq 0.884$) remain path independent up to a certain load which is attributed to crack initiation, and then diverge. There is a unique signature of the strain energy density (dW/dV) ahead of the crack in the 0° direction: the strain energy first decreases, reaches a minimum and then increases with increasing distance from the crack tip. The minimum strain energy shows a unique dependence on the applied load. This leads to the prediction of the fracture loads for the cracked specimens.

A novel coordinate system rotation was employed in extracting the boundary conditions from the two-dimensional global model to the three-dimensional local model for the local-global finite element analysis of the unidirectional composite. The mechanics of load transfer and the subsequent fracture and were studied over a range of interface strengths (138 - 934 MPa). The analysis leads to the prediction of debonding between fiber and matrix. The degree of load transfer from the matrix to the fiber was found to depend upon both the angular orientation and distance from the crack front. An optimum value of the interface strength, $(\sigma_i)_{opt}$ has been established for the composite for its maximum load bearing capability.

TABLE OF CONTENTS

LIST OF TABLES	vi
LIST OF FIGURES.....	vii
NOMENCLATURE.....	xi
ACKNOWLEDGEMENTS	xiv
Chapter 1. INTRODUCTION TO MICROMECHANISMS OF FRACTURE IN COMPOSITES.....	1
Elastic-Plastic Analysis of Fracture.....	2
Toughness <i>versus</i> Work of Fracture in Metal Matrix Composites	4
Energy Absorbing Micromechanisms.....	5
Fiber pull-out.....	7
Crack bridging.....	8
Crack deflection.....	9
Fiber breakage	12
Micromechanical Modeling.....	12
Analytical Formulations.....	13
Vanishing fiber diameter model.....	13
Aboudi model	13
Cox model.....	14
Paul model.....	15
Computational Finite Element Analysis.....	16
Continuum approach	16
Micromechanics approach	18
Objective and Scope of the Investigation	21
Chapter 2. NUMERICAL PROCEDURE	22
Fracture of Monolithic Metals.....	22
Capabilities of PAPST	22
Modifications Made to PAPST.....	24
Additional Postprocessors.....	24
Solution Procedure	25

Materials Under Investigation.....	25
Local-Global Micromechanical Modeling.....	25
Material Properties.....	29
Numerical Approach	29
Chapter 3. RESULTS AND DISCUSSION	38
Monolithic Materials.....	38
Mesh Deformation.....	39
Strain Energy Density.....	39
Crack Tip Plasticity.....	45
Metal Matrix Composites	57
Macro-Mechanics Analysis.....	57
Micro-Mechanics Analysis	62
Chapter 4. SUMMARY AND CONCLUSIONS	75
Chapter 5. RECOMMENDATIONS FOR FUTURE WORK.....	77
REFERENCES.....	78
APPENDIX A. J-INTEGRAL CUTTING PROGRAM.....	85
APPENDIX B. POSTSCRIPT CONNECTIVITY PROGRAM.....	87
APPENDIX C. PROGRAM LISTING OF 2-D ORTHOTROPIC PROBLEM	90

LIST OF TABLES

Table 2.1.	Compact tension specimen geometry and material data	27
Table 2.2.	Compiled properties of fiber, matrix and composite for SCS-6/Ti-15-3 system (properties extracted from reference 48).....	30

DTIC QUALITY INSPECTED 1

Accession For	
NTIS GRAB	<input checked="" type="checkbox"/>
DTIC TAB	<input type="checkbox"/>
Unannounced	<input type="checkbox"/>
Justification	
Distribution/	
Availability Codes	
Dist	Avail and/or Special
A-1	

LIST OF FIGURES

Figure 1.1.	Schematic of the crack tip process zone in a continuous fiber metal matrix composite showing distinct energy absorbing mechanisms.	6
Figure 1.2.	Delamination chart showing the mechanism of composite failure (extracted with permission from the unpublished work of Gupta and Argon [14])	11
Figure 1.3.	Coordinate system used in deriving longitudinal stiffness of the Cox model.....	15
Figure 2.1.	Flowchart for analyzing elastic-plastic fracture problems using the modified <i>ARLPAPST</i> finite element code.....	26
Figure 2.2.	True stress-strain curves of HY-130 steel, HY-140 steel and 5083-O aluminum and 7075 aluminum.	28
Figure 2.3.	Nonlinear stress-strain curve used to model titanium 15-3 matrix material on the local level.....	31
Figure 2.4.	Schematic of the macroscopic model showing boundary conditions, fiber orientation and specimen dimensions.	32
Figure 2.5.	Representative unit cell distinguishing fiber, matrix and interphase of a 0.325 volume fraction SiC/Ti composite. The fiber is modeled as elastic, while the matrix is elastoplastic. Gap elements are used to simulate the interfacial region.	34
Figure 2.6.	Pictorial flowchart showing the global model in parts A and B and the local model in parts C and D. Note that the global model is 2-dimensional and that the local model is 3-dimensional.....	36
Figure 2.7.	Nodal plot of the global model near the crack tip region. The outlined section represents the dimensions of the local model superimposed upon the figure.....	37
Figure 3.1.	Picture showing the deformed upper half of a compact tension specimen model constructed of 5083-O aluminum. The crack tip ($a=3.199$ in) is located as shown.	40
Figure 3.2.	Picture showing the deformed upper half of a compact tension specimen model constructed of 7075 aluminum. The crack tip ($a=1.537$ in) is located as shown.	41
Figure 3.3.	Strain energy density plotted against the radial distance from the crack tip in HY-130 steel ($a=1.537$ in).	42

Figure 3.4.	Strain energy density plotted against the radial distance from the crack tip in 5083 aluminum ($a=3.199$ in).....	43
Figure 3.5.	$(dW/dV)_{min}$ plotted against applied load for three crack lengths in HY-13C stainless steel ($a=1.537$ in, 1.623 in and 1.7685 in) two crack lengths in 7075 aluminum ($a=1.537$ in and 1.623 in) and one crack length in 5083 aluminum ($a=3.199$ in). Fracture load is determined by extrapolating curve to the load axis.	44
Figure 3.6.	Contour plot of the Von Mises effective stress (psi) in 5083-O aluminum ($a=3.199$ in). The model is shown to scale in inches.	46
Figure 3.7a.	Contour plot of the Von Mises effective stress (psi) in 7075 aluminum ($a=1.537$ in). The model is shown as 2:1 in inches.	47
Figure 3.7b.	Contour plot of the Von Mises effective stress (psi) in 7075 aluminum ($a=1.623$ in). The model is shown as 2:1 in inches.	48
Figure 3.8a.	Contour plot of the Von Mises effective stress (psi) in HY-130 steel ($a=1.537$ in). The model is shown as 2:1 in inches.	49
Figure 3.8b.	Contour plot of the Von Mises effective stress (psi) in HY-130 steel ($a=1.623$ in). The model is shown as 2:1 in inches.	50
Figure 3.8c.	Contour plot of the Von Mises effective stress (psi) in HY-130 steel ($a=1.7685$ in). The model is shown as 2:1 in inches.....	51
Figure 3.9.	Variation of J along the crack tip ligament for 7075 aluminum ($a=1.537$ in). Note the variation of J is small until the load is increased beyond P^* . Note that $1 \text{ in}^* \text{lb/in}^2 = 0.17513 \text{ kJ/m}^2$	52
Figure 3.10.	Variation of J along the crack tip ligament for 7075 aluminum ($a=1.623$ in). Note the variation of J is small until the load is increased beyond P^* . Note that $1 \text{ in}^* \text{lb/in}^2 = 0.17513 \text{ kJ/m}^2$	53
Figure 3.11.	Variation of J along the crack tip ligament for HY-130 steel ($a=1.623$ in). Note the variation of J is small until the load is increased beyond P^* . Note that $1 \text{ in}^* \text{lb/in}^2 = 0.17513 \text{ kJ/m}^2$	54
Figure 3.12.	Variation of J along the crack tip ligament for HY-130 Steel ($a=1.7685$ in). Note the variation of J is small until the load is increased beyond P^* . Note that $1 \text{ in}^* \text{lb/in}^2 = 0.17513 \text{ kJ/m}^2$	55

Figure 3.13.	J versus applied load for aluminum and structural steel alloys.....	56
Figure 3.14.	Optimization of finite element mesh for global model considering the effective stress at a radius of 3.74 mm away from the crack tip. The material system is SCS-6/Ti-15-3.....	58
Figure 3.15.	Effective stress contour plot in 255 element macroscopic model. The plate is modeled using quarter symmetry, the crack tip is located in the lower left corner.....	59
Figure 3.16.	Effective stress contour plot in 456 element macroscopic model. The plate is modeled using quarter symmetry, the crack tip is located in the lower left corner.....	60
Figure 3.17.	Displacements obtained from the solution of the global model. The data are interpolated using polynomial fits on layers D and C, while visual interpolation is used on layers B and A (refer to Fig 2.7).....	63
Figure 3.18.	Displacements obtained from the solution of the global model. The data are interpolated using polynomial fits on all layers (refer to Fig. 2.7).....	64
Figure 3.19.	Deformed finite element mesh showing fiber debonding in SCS-6/Ti-15-3. Crack plane is outlined as shown.....	65
Figure 3.20.	Effective stress contour is SCS-6/Ti-15-3 when $\sigma_i = 934$ MPa. Note that the stresses are concentrated within the fiber due to effective load transfer.	66
Figure 3.21.	Plot of the effective stress against the radial distance from the crack tip in the normal direction to the crack front.	68
Figure 3.22.	Schematic cross section of micro-model showing right hand definite angular orientation. Fiber A corresponds to the broken fiber, while fibers B and C remain unbroken	69
Figure 3.23.	Part A shows effective load transfer in fibers A, B and C as a function of angular orientation on the crack plane. Part B shows effective load transfer on the plane furthest from the crack plane. The interface strength is 934 MPa.	70
Figure 3.24.	Part A shows effective load transfer in fibers A, B and C as a function of angular orientation on the crack plane. Part B shows effective load transfer on the plane furthest from the crack plane. The interface strength is 534 MPa.	71

- Figure 3.25. Part A shows effective load transfer in fibers A, B and C as a function of angular orientation on the crack plane. Part B shows effective load transfer on the plane furthest from the crack plane. The interface strength is 138 MPa.72
- Figure 3.26. Optimization of the interface strength considering the stress in the matrix near the fiber-matrix interface. The optimum value of the interface strength, $(\sigma_i)_{opt}$, may be obtained by reading the interface strength at the intercept of the two curves.73

NOMENCLATURE

\bar{K}	Stiffness matrix
$\Delta \bar{a}$	Boundary displacement
\dot{e}_{ij}	Deviatoric strain rate components
\dot{s}_{ij}	Deviatoric stress rate components
\bar{B}	Displacement-strain matrix of the equivalent homogeneous volume
\bar{L}	Overall equivalent homogeneous volume instantaneous stiffness matrix
$\frac{dW}{dV}$	Strain energy density
α	Constant term (Weibull distribution)
a	Crack length
β	Constant term (Weibull distribution)
COD	Crack opening displacement
d	Fiber diameter
δ_o	Crack opening displacement
$\Delta \Pi$	Energy change
E_f	Young's modulus of the fiber
E_{ij}	Tensorial stiffness matrix
ϵ_{ij}	Strain tensor
ϵ_o	σ_o/E
E_p	Young's modulus of the particle
$f(\sigma)$	Probability of fiber failure
G	Global solution matrix

G_m	Shear modulus of the matrix
h	Ratio of flawed to unflawed fiber strength
H_{11}	$[2n\lambda^{1/4}\sqrt{S_{11}S_{22}}]_1 + [2n\lambda^{1/4}\sqrt{S_{11}S_{22}}]_2$
H_{22}	$[2n\lambda^{-1/4}\sqrt{S_{11}S_{22}}]_1 + [2n\lambda^{-1/4}\sqrt{S_{11}S_{22}}]_2$
I_n	Normalizing constant
J	Measure of the intensity of the elastic-plastic stress-strain field that surrounds the crack tip
K	Measure of the intensity of the elastic stress-strain field that surrounds the crack tip
K_C	Measure of composite toughness
K_{IC}	Plane strain fracture toughness
K_Q	Measure of composite toughness
l	Fiber length
λ	S_{11}/S_{22}
l/d	Aspect ratio
l_c^*	Critical fiber length, $(\sigma_{fb} - \sigma_{fb}^*)l_c/\sigma_{fb}$
L^k	Overall representative volume element subelement instantaneous stiffness matrix
ν	Poisson's ratio
N	Number of nodes
n	Strain hardening exponent
P^*	Defined load at which $(dW/dV)_{min}$ reaches its maximum value
ρ	$(2S_{12} + S_{12})/2(S_{11}S_{22})^{1/2}$
r_o	Average whisker radius
r_p	Plastic zone radius

s^*	Lower limiting strength
σ_e	Von Mises effective stress
σ_e'	Von Mises effective stress with respect to the coordinates of the current center of the yield surface
σ_f	Average fiber stress away from the crack plane
$(\sigma_i)_{opt}$	Optimum value of the interface strength
σ_{fb}	Unflawed fiber strength
σ_{fb}^*	Flawed fiber strength
S_{ij}	Tensorial compliance matrix
s_{ij}	Current deviatoric stress components
σ_{ij}	Stress tensor
s_{ij}'	Deviator stress components measured from the center of the current yield surface
S_{max}	Distortional component of the strain energy density
S_{min}	Dilatational component of the strain energy density
σ_o	Yield stress (Ramberg-Osborn relation)
τ_i	Matrix-fiber interfacial shear strength
V_f	Volume fraction of reinforcing fibers
V_p	Particle volume fraction
W_p	Plastic work
W_{po}	Work required to pull out a fiber

CHAPTER 1

INTRODUCTION TO MICROMECHANISMS OF FRACTURE IN COMPOSITES

The micromechanisms of fracture in polymeric, metallic or ceramic composite materials reinforced with strong, stiff fibers interact in a complex manner. These include, but are not limited to, matrix and fiber cracking, crack bridging, delamination and crack deflection. Metal matrix composites present the additional problem of yielding and plastic deformation in localized regions. Depending on the composite system under investigation, the interface will affect the stress distribution around a loaded crack tip. In the past, work has centered on experimental observations of the micromechanical causes of damage [1-2], closed form analytical procedures designed to calculate laminate mechanical properties and damage accumulation [3-8], characterization of the interphase region through finite element analysis and complex constitutive relations [9-14], and local-global finite element calculations of cracked composites [15-17].

A broad base of knowledge is required to analyze damage in composite materials. Some background on elastic-plastic fracture mechanics will first be given to comprehend how plasticity plays a role on both the microscopic and macroscopic levels. Next, the metallurgical and composite damage mechanisms in these composites will be categorized and quantified to account for the multiple energy absorbing mechanisms. Finally, a state of the art review will be given on analytical and computational micromechanical modeling techniques.

Elastic-Plastic Analysis of Fracture

As noted by Orowan [18], the work required to fracture ductile, tough metal is greatly increased due to an additional plastic deformation work (γ_p). This deformation is absorbed through a process of microvoid nucleation, growth and linking.

Microscopically these voids may begin to form in individual grains at stresses much lower than the yield point. Depending the strain hardening and strain rate hardening of a material, void nucleation and growth may occur homogeneously in areas of high dislocation densities or may occur heterogeneously along grain boundaries or particle inclusions [19]. Conversely, the plastic deformation of the metal on a large scale can be experimentally observed on pre-polished and loaded samples as variations in the material's surface roughness. Lee [20] found that the intensity of reflected light is linearly related to the surface roughness, which is directly proportional to the effective strain. This allows for an accurate measurement of the crack tip plastic zone size. Numerical analyses have been performed verifying the extent of plastic deformation on globally isotropic material models. Criteria such as the J -Integral are then used to characterize the crack tip process zone.

Rice's J -Integral [21] has been formulated as a possible fracture criterion for materials that exhibit nonlinear stress-strain behavior. J has been shown to accurately predict crack initiation in structural alloys [22,23] and has been studied numerically as it applies to limited crack extension (dJ/da) [24-28]. The need for a ductile fracture criterion stems from the inherent plasticity that surrounds a crack tip prior and during crack growth, thus exceeding the approximations used in linear elastic fracture mechanics (LEFM). Elastic-plastic fracture mechanics (EPFM) must be employed when the crack tip plastic zone (CTPZ) is large compared to the dimensions of the specimen. Fracture parameters such as the crack tip opening displacement measurement (CTOD)

and analytical solutions of the slip-line field have been studied as they relate to ductile instability and have met with some success [29]. From the work of Hutchinson [30], Rice and Rosengren [31], the stresses, strains, and displacements are known within a radius, r_p , from the crack tip in the case of large scale and general yielding for linear hardening elastic-plastic materials. This zone is the so-called HRR zone (taken from the work of Hutchinson, Rice and Rosengren), while the material outside the crack tip plastic zone remains in the elastic region. The stresses and strains within the HRR zone may be described by the following equations:

$$\sigma_{ij} \sim \sigma_o \left[\frac{J}{\beta \epsilon_o \sigma_o I_n r} \right]^{1/(n+1)} \tilde{\sigma}_{ij}(\theta, n) \quad (1.1)$$

$$\epsilon_{ij} \sim \beta \epsilon_o \left[\frac{J}{\beta \epsilon_o \sigma_o I_n r} \right]^{n/(n+1)} \tilde{\epsilon}_{ij}(\theta, n) \quad (1.2)$$

$$u_i - u_i^o \sim \beta \epsilon_o r \left[\frac{J}{\beta \epsilon_o \sigma_o I_n r} \right]^{n/(n+1)} \tilde{u}_i(\theta, n) \quad (1.3)$$

The constants β , ϵ_o , σ_o come from the Ramberg-Osgood description of a material's stress strain curve described by the following relationship:

$$\frac{\epsilon}{\epsilon_o} = \beta \left(\frac{\sigma}{\sigma_o} \right)^n \quad (1.4)$$

The work of Hutchinson, Rice and Rosengren gained recognition due to the variety of problems that could be described by the so-called HRR zone located near a loaded crack tip of ductile materials. Attempts to solve for the stresses and strains

within metals exhibiting power law hardening proved to be intractable in closed form solution and finite element analysis was then used to solve these types of problems.

In the past, the path independence of J has been established, excluding contours that pass through dissimilar media, holes or drastic dimensional changes or where a large amount of crack extension takes place [32]. The stress intensity factors K and J are only applicable if they uniquely characterize σ_{ij} and ϵ_{ij} at the location of fracture initiation [33]. It has been shown analytically that the J -dominated HRR region is valid up to 0.25 times the length of the plastic zone radius [34-37]. Thus the J -Integral has been used to study fracture problems involving plasticity beyond the scope of LEFM based on the K concept [38].

An alternative fracture criterion has been proposed by Sih [39-40] which is capable of predicting the critical crack initiation load as well as the crack propagation direction. By measuring the amount of strain energy absorbed by a material in front of a crack tip, the strain energy density factors S_{min} and S_{max} may be calculated, which refer to dilatation (local volume changes) and distortion respectively. The critical value of S_{min} may then be used as a failure criterion to predict the failure load of sharply defined cracks or elliptical notches.

Toughness *versus* Work of Fracture in Metal Matrix Composites

Several authors [41-42] have pointed out that characterizing the plane strain fracture toughness (K_C or K_{IC}) in composite materials is not as straight forward as in isotropic metals. The inherent anisotropy of composite materials makes the fracture mode mixed, even under simple tension. ASTM has established rigorous testing procedures (E399) to measure the inherent fracture toughness of quasi-brittle materials;

however, a standardized test method for MMCs has not yet been developed. Friend [41] points out that K_C is not a measure of the material's homogeneous fracture toughness since continuous fiber metal matrix composites are highly anisotropic. Fracture toughness will be used in reference to the parameter rigorously established by ASTM E399 and "toughness" will be used in reference to a measure of the materials ability to absorb energy.

An alternative method of measuring the "toughness" of composite materials is by measuring the fracture energy or work of fracture. The following definition has been given by Davidson [42], ". . . work of fracture--the dissipation of the elastic energy imposed in the specimen by the externally applied load per unit of new crack surface formed." This measure of toughness may be obtained by calculating the area under a load-crack opening displacement (*COD*) curve during 3 point bend, or the area under the force-time curve in an impact test. Magata and Hall [43] have measured the area under the load-*COD* curve, and found radically different values of toughness as compared to K_Q for their α - $\text{Al}_2\text{O}_3/\text{Mg}$ system. Specifically, K_Q is defined as the experimentally determined value of the toughness of the composite that does not satisfy ASTM standard E399. For composite materials it may be appropriate to measure the toughness using both methods.

Energy Absorbing Micromechanisms

Pictured in Fig. 1.1 is the crack tip process zone or "local heterogeneous region" in a continuous fiber MMC. Within the schematic are numerous mechanisms that contribute to the total fracture in a fiber composite containing a distinct interfacial region. The mechanisms are as follows: 1) fiber pull-out, 2) crack bridging, 3) crack deflection, 4) fiber breakage, and 5) matrix yielding and plasticity. Each mechanism will be treated

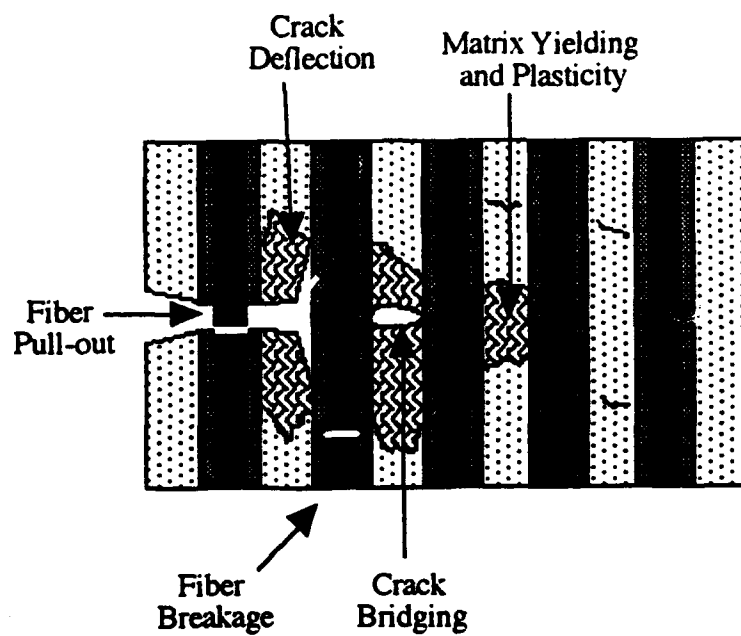


Figure 1.1. Schematic of the crack tip process zone in a continuous fiber metal matrix composite showing distinct energy absorbing mechanisms.

separately in detail, with the exception of matrix yielding and plasticity, which has been previously discussed.

Fiber pull-out

Additional energy is expended during fiber pull-out, thus by increasing the pull-out length, additional toughness may be gained. In the analysis given by Taya and Arsenault [44], the average pull-out energy per unit area, \overline{W}_{po} , is given as follows:

$$\overline{W}_{po} = \frac{V_f \tau_i l^2}{6 d} \quad \text{for } l < l_c^* \quad (1.5)$$

$$\overline{W}_{po} = \frac{(1-\eta)^3 V_f \tau_i l^3}{6 d l} \quad \text{for } l > l_c^* \quad (1.6)$$

The maximum pull-out energy $\overline{W}_{po_{max}}$ is given when $l=l_c^*$:

$$(\overline{W}_{po})_{max} = \frac{V_f d \sigma_{fb}^2}{24 \tau_i} \quad (1.7)$$

Equation 1.7 shows that the maximum energy is expended in pulling out fibers given high volume fractions, large diameter fibers, high fiber strengths and low interfacial strengths.

Due to the desire to retain strength and stiffness, the bonding between fiber and matrix is relatively high. Systems such as α -Al₂O₃/Mg [43], Boron/Al [45-46] and SiC/Al [47] possess good chemical bonding and experience mechanical clamping due to the differences in thermal expansion coefficients between the fiber and matrix. These composites are not likely to exhibit fiber pullout. However, composites such as SCS-

6/Ti-15-3 exhibit extremely poor interfacial bonding and large amounts of fiber pull-out [48]. To promote fiber pull-out, Magata and Hall [43] thermally cycled their α - $\text{Al}_2\text{O}_3/\text{Mg}$ composite to debond the fibers from the matrix consequently lowering the degree of interfacial bonding. Although the measured values of K_Q decreased from 22.7 to 9.1 $\text{MPa}\sqrt{\text{m}}$ when tested in the longitudinal direction, the work-of-fracture increased from 0.202 to 0.354 J from the uncycled to the cycled conditions. The 75% increase in work-of-fracture would have gone unnoticed if both experiments had not been conducted.

Crack bridging

In the case when the matrix separates ahead of the crack tip and the fibers are exposed or "bridge" the crack, additional energy is required for crack propagation [44]. The additional plastic work (W_p) performed on the matrix by the fibers during crack bridging is given by:

$$\overline{W_p} = \pi d^2 (\sigma_{fb} - \sigma_f) \delta \ell / 2 \quad (1.8)$$

This phenomenon was highly noticeable in an $\text{Al}_2\text{O}_3/\text{Al}$ composite formed through the Lanxide® process [49]. Although the reinforcement was discontinuous, crack bridging added to the toughness in the presence of lower volume fractions of alumina. In order for the composite to exhibit crack bridging, a favorable stress state must be present. Increasing triaxiality would, in effect, favor the rapid nucleation of microvoids. Averbuch and Hahn [46] noted that the presence of boron fibers in an aluminum matrix acted to increase the triaxial stress state ahead of the crack tip, which could be seen from the large regions of plastic deformation.

Crack deflection

Irregular crack paths expend greater energy than self-similar cracks due to the decreased stress concentration at the crack tip. This may be directly caused by deflected crack propagation in angle ply composites or interfacial crack propagation in unidirectional composites. An indirect effect of the irregular crack path is crack closure, which shields the crack tip thus reducing the effective stress concentration. The irregular crack paths significantly increase the toughness in B/Al [45] and α -Al₂O₃/Al [43]. Mahulikar et al. [2] have shown that fiber orientation plays an important role on the failure mode of B₄C and SiC/Ti-6-4 metal matrix composites. Self-similar crack propagation consisting of transfibral and interfacial failures occurs when the crack is oriented at an angle greater than 45° to the fiber direction. If the properties of the interface are altered by thermal cycling, then failure occurs primarily along the interface. Thermal cycling forms reaction products along the interface creating a "band of weakness" in which failure is favored. Clearly the degree of interfacial bonding is related to the amount of crack deflection.

Recent analytical work by Gupta and Argon [14] on brittle composite interfaces suggests that fiber breakage or delamination can be controlled by varying the elastic constants of both the interphase and the fiber. This work has been made possible through new techniques of measuring the material properties of the fiber and interphase using a unique laser spallation technique [50]. The earliest reference to this type of work can be traced back to studies of cracks adjacent to bimaterial interfaces. Gupta and Argon use the following parameters λ and ρ to define the degree of anisotropy in these composites:

$$\lambda = \frac{S_{11}}{S_{22}} \quad (1.9)$$

$$\rho = \frac{2S_{12} + S_{16}}{2\sqrt{S_{11}S_{22}}} \quad (1.10)$$

These parameters (λ and ρ) form the basis of the Dundur's parameters α and β [14] as is given below:

$$\alpha = \frac{(\sqrt{S_{11}S_{22}})_c - (\sqrt{S_{11}S_{22}})_f}{(\sqrt{S_{11}S_{22}})_c + (\sqrt{S_{11}S_{22}})_f} \quad (1.11)$$

$$\beta = \frac{(\sqrt{S_{11}S_{22}} + S_{12})_2 - (\sqrt{S_{11}S_{22}} + S_{12})_1}{H_{11}H_{22}} \quad (1.12)$$

$$n = \sqrt{\frac{1+\rho}{2}} \quad (1.13)$$

$$m = \sqrt{\frac{1-\rho}{2}} \quad (1.14)$$

The Dundurs parameters β and ρ remain relatively constant when values of the elastic constants for typical engineering materials are substituted. The final dependence for the generalized delamination chart falls onto a choosing $\rho_1=1$, $\rho_2=1$, $\lambda_2=1$ and $\lambda_2=1$. By plotting α against the ratio of the applied transverse stress to the strength of the interface, the failure mode of the material may be predicted (see Fig 1.2). Above the constructed line, cracks will deflect along the interface, while the lower region will result in fiber failure. Knowing the elastic constants of the interface and the fiber, the ratio of the transverse strength to the longitudinal strength may be calculated. In this manner, delamination charts were analytically formulated to engineer composite materials that

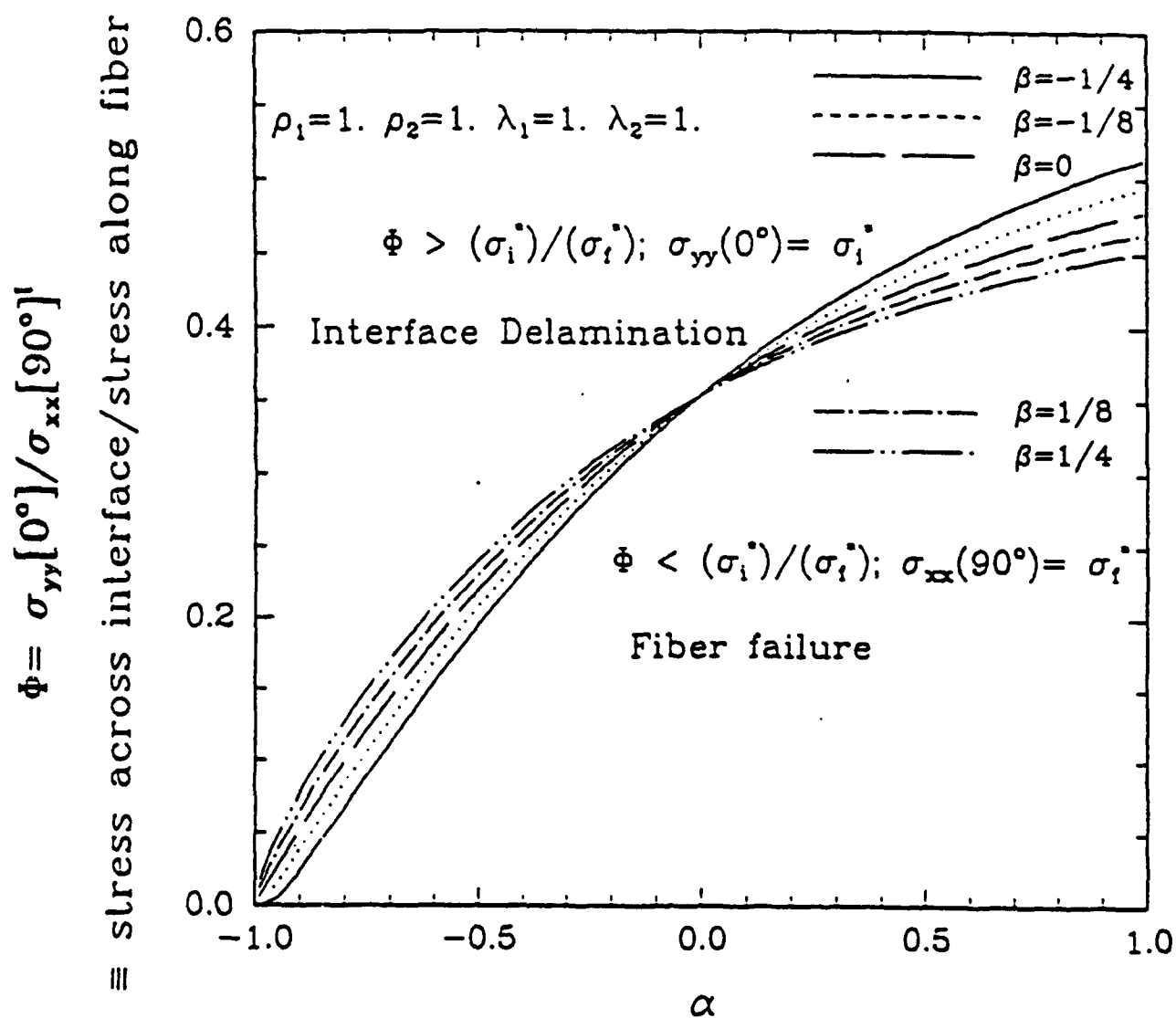


Figure 1.2. Delamination chart showing the mechanism of composite failure (extracted with permission from the unpublished work of Gupta and Argon [14]).

provide both high transverse and longitudinal strength as well as high toughness (fiber pull-out). Through such processes as CVD and PVD, the elastic properties of the interface may be tailored to suit a specific application.

Fiber breakage

The ultimate strength of a CFM is highly dependent upon the strength of the individual fibers. The strength of these fibers, unlike that of the metal matrices, is statistical in nature and may be described using Weibull statistics. The less scatter in strength the fibers possess, the easier it is to predict the failure of a fibrous composite. Such a distribution can be given by the following relation [44]:

$$f(\sigma_{fb}) = l\alpha\beta \exp\{-l\alpha\sigma_{fb}^\beta\} \quad (1.15)$$

Micromechanical Modeling

Micromechanical modeling can be broken into two areas of interest: analytical modeling and finite element analysis. Analytical modeling makes simplifying assumptions of the material's behavior yielding constitutive equations in closed form. Finite element analysis solves for the stresses and strains of a discretized model numerically. Both methods have their advantages and disadvantages. Analytical models provide mathematically simple equations that can be used for design, but often at the expense of realism. Under careful scrutiny, finite element analysis can yield reliable solutions, but may require large amounts of computer resources.

Analytical Formulations

To date, there has been a significant amount of work performed on determining the mechanical properties of composites from the properties of the constituents. Hashin [51] has categorized analytical procedures into three areas: the direct approach, the variational approach and approximation techniques. These procedures may be applied to statistically isotropic (particulate) composites as well as to fibrous composites. Of these approaches, only the models using the direct approach will be considered. The direct approach yields an exact solution of the effective properties of a composite considering a geometric model. Below are highlighted some popular micromechanical models that are relevant to metal matrix composites.

Vanishing fiber diameter model

This model was developed by Dvorak and Bahei-El-Din [52,53] specifically for analyzing micromechanical problems in metal matrix composites. The model was evaluated using the 2-dimensional laminate AGLPLY program by Bigelow and Naik [15]. The values of the longitudinal modulus and Poisson's ratio were found to be within 6% of the experimentally determined values in the B/Al and SiC/Ti [0]_g laminates. Although AGLPLY was designed to predict the laminate response, individual constituent stresses can be calculated. It was found that the constituent stresses developed by mechanical loads were more accurate than stresses developed by thermal loads when compared to finite element calculations [15].

Aboudi model

The Aboudi model [54,55] is capable of describing the effective behavior of elastoplastic composites. The periodic and geometrical arrangements of rectangular

parallelepipeds in the Aboudi model allow both continuous fiber and particulate composites to be studied. The nonlinearity of the metal matrix has been accounted for using elastoplastic temperature dependent constitutive relations. The complex derivation and results are too lengthy to discuss in detail here. For the complete derivation and constitutive relations, see reference 54.

Cox model

The Cox model, as summarized by Johnson and Birt [56], was designed to analyze short fiber systems. This model accounts for the shear and axial stress distribution along an embedded fiber. The Cox model also derives the longitudinal stiffness as given in equations (1.16-1.20) according to the coordinate system shown in Fig. 1.3.

$$E = E_f V_f \left[1 - \frac{\tanh\left(\frac{\beta l}{2}\right)}{\frac{\beta l}{2}} \right] + E_m (1 - V_f) \quad (1.16)$$

$$\tau = E_f \epsilon \sqrt{\frac{G_m}{2E_f \ln[1/\sqrt{V_f}]}} \frac{\sinh \beta((l/2) - x)}{\cosh \beta(\beta l/2)} \quad (1.17)$$

$$\sigma = E_f \epsilon \left(\frac{1 - \cosh \beta((l/2) - x)}{\cosh \beta(\beta l/2)} \right) \quad (1.18)$$

$$\beta = \sqrt{H/E_f \tau_o^2} \quad (1.19)$$

$$H = 2\pi G_m / \ln[1/\sqrt{V_f}] \quad (1.20)$$

In their evaluation, Johnson and Birt found the Cox model accurately predicted longitudinal stiffness. However, the Cox model should not be used for very short fiber composites ($l/d \leq 4$) or for particulate composites due to inadequate load transfer through shear.

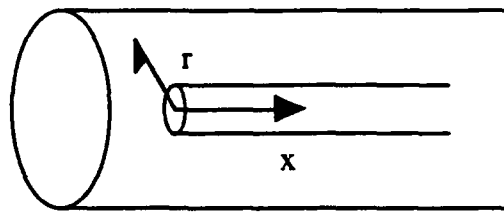


Figure 1.3. Coordinate system used in deriving longitudinal stiffness of the Cox model.

Paul model

The Paul model was derived to predict the elastic modulus of particulate composite materials. This model assumes that the Poisson's ratio of the matrix equals that of the reinforcement and that the strain in the matrix equals the strain seen by the particles. The transverse and longitudinal elastic moduli are given in equation (1.21).

$$E_{22} = E_{11} = \frac{E_m[E_m + (E_p - E_m)V_p^{2/3}]}{E_m + (E_p - E_m)V_p^{2/3}(1 - V_p^{1/3})} \quad (1.21)$$

Johnson and Birt [56] found that the Paul model predicted an upper bound of elastic moduli in particulate metal matrix composites, but should not be used for whisker reinforced metals.

Computational Finite Element Analysis

The finite element method (FEM) has been the solution procedure of choice for complex problems involving mechanical and hygrothermal loading of composite materials [48,57-64]. This method has been applied to brittle [57,58] and ductile matrix [59-63] composites. Current and past computational studies of composite materials can be separated into two levels: a continuum or global level and a micromechanical or local level. Some investigators have chosen to link these regimes through a local-global analysis where the global stress state and loading history dictates the boundary conditions for the local model. In the following sections, both levels of analysis will be described along with example case studies.

Continuum approach

The object of a global analysis is to describe the overall mechanical response of a composite structure. The material is considered statistically homogeneous down to the ply level. Several finite element codes have been written to account for fibrous reinforcement and laminate design.

Aboudi's vanishing fiber diameter (VFD) model and the plasticity theories developed by Dvorak and Bahei-El-Din [52,53] inspired codes such as PAC78 and PAFAC. NASA researchers [6,15,62] have used these codes to observe strain distributions ahead of geometrical discontinuities (such as notches and holes). Relatively good comparisons with experimental results were noted.

The three-dimensional package, PAFAC, has been extensively used in studying boron/aluminum and silicon carbide/aluminum systems [15,62]. The eight noded hexahedral elements represent a composite continuum incorporating matrix and fiber failure theories. The following equation predicts fiber failure in PAFAC:

$$\left(\frac{\sigma_{11}^f}{\sigma_{11}^{ult}}\right)^2 + \left(\frac{\sigma_{12}^f}{\sigma_{12}^{ult}}\right)^2 \geq 1 \quad (1.22)$$

Where σ_{11} is the tensile stress in the fiber direction and σ_{12} is the shear stress.

An ultimate strain criterion is used to calculate matrix failure:

$$(\epsilon_{22}^m)^2 + (\epsilon_{11}^m)^2 - \epsilon_{11}^m \epsilon_{22}^m + 3(\epsilon_{12}^m)^2 \geq \epsilon_m^u \quad (1.23)$$

In a study of SCS-2/6061 Al, Johnson and Bigelow [62] noted good prediction of the normalized strains ahead of a slit in $[0/90]_{2s}$ laminates. The numerical predictions from PAFAC were compared to results obtained with an array of five strain gages positioned ahead of the notch. In $[\pm 45]_{2s}$ laminate poor correlation was found, possibly due to fiber rotation and interlaminar yielding.

To overcome possible interlaminar nonlinearity, Hinrichsen and Palozotto [65] have devised a cubic spline function. In effect, the assumption of plane sections remaining plane is eliminated. This has been a problem in thick plate applications. In

the past, thin shell elements have been "artificially softened" to simulate real life applications, whereas Hinrichsen and Palozotto have generated accurate results without empirically reducing G_{13} and G_{23} .

A final application of continuum FEA concerns predicting the mechanical properties of laminates. Johnson et al. [48] have used AGLPLY, a code employing Aboudi's plasticity theories, for predicting the elastic/plastic behavior of symmetric composite plates supporting in-plane loads. AGLPLY has successfully predicted overall laminate moduli, ply stresses and strains throughout the loading history.

Micromechanics approach

A more desirable approach would be to predict the composites mechanical properties based only on the mechanical properties of the individual constituents. In the next segment, three representative micromechanics approaches will be discussed. Each uses the material properties of distinct fiber and matrix regions. Dvorak and Teply [61] developed an ingenious energy balance method to predict instantaneous composite stiffness, while Lerch and Melis [66] used a straight ahead approach to describe the stress state and slip band regions in cross ply laminates. Pagano and Tandon [64,67] utilized a 3-cylinder assemblage model to study the effects of various coatings on the stress distribution around a thermally loaded fiber.

On a micromechanical scale, it is important to establish a working representative volume element (RVE) which accurately represents the composite. The only models for which mathematically precise solutions may be obtained are the composite cylinder assemblage and periodic arrays of identical fibers. The former may be solved analytically, while the latter must be solved numerically. To date, a variety of periodic fiber arrays have been used to determine mechanical property data for composite materials.

Dvorak and Teply [61] have presented a guideline that should be used to construct accurate representative volume elements: a) when repeated it continuously covers the entire macroscopic volume of the composite and b) when loaded by uniform stresses or strains, the local stresses and strains are identical within each RVE in the macroscopic volume. Likewise, they represent the macroscopic composite by an equivalent homogeneous volume (EHV) element. By equating the energy changes in the RVE and the EHV when subjected to the identical boundary conditions, they determine the instantaneous stiffness of the EHV. The energy change ($\Delta\Pi$) from a known solution state to a slightly perturbed state has been derived for the RVE and the EHV:

$$\Delta\Pi_{EHV} = \Delta\bar{\Pi} = \frac{1}{2} \Delta\bar{a}^T \bar{B}^T \bar{L} \bar{B} \Delta\bar{a} - \Delta\bar{\sigma}^T \bar{B} \Delta\bar{a} \quad (1.24)$$

$$\Delta\Pi_{RVE} = \Delta\Pi = \frac{1}{2} \Delta\bar{a}^T \bar{K} \Delta\bar{a} - \Delta\bar{F}^T \Delta\bar{a} \quad (1.25)$$

Through boundary conditions applied to the RVE and EHV, Dvorak and Teply accurately predicted upper and lower bounds of elastic moduli using ABAQUS. Displacement or strain was applied to the EHV to give an upper bound estimate, while stress or traction was applied to give a lower bound estimate. The instantaneous stiffness L of the macroscopic composite is at this point unknown. Next, the identical boundary conditions were applied to the RVE having known instantaneous stiffness L_i (i represents the fiber and matrix). The energy terms in both the local and global models were then equated to determine L_{global} . The following formula was used by Dvorak and Teply to determine the energy change, $\Delta\Pi$, for an upper bound estimate using a displacement approximation:

$$\Delta \bar{\pi} = \int_V \int_{\bar{\epsilon}}^{\bar{\epsilon}_n + \Delta \bar{\epsilon}} \bar{\sigma}^T d\bar{\epsilon} dV \int_{S_f} \int_{\bar{u}}^{\bar{u}_n + \Delta \bar{u}} \bar{i} d\bar{u} dS \quad (1.26)$$

The equilibrium model was then used for determining a lower bound estimate:

$$\Delta \bar{\pi}_c^e = \int_{V^*} \int_{\sigma}^{\sigma_n + \Delta \sigma} \bar{\epsilon}^T d\bar{\sigma} dV \int_{S_u^*} \int_{\bar{i}}^{\bar{i}_n + \Delta \bar{i}} \bar{u}^T d\bar{i} dS \quad (1.27)$$

Energy principles were used to show the upper and lower bound estimates. Dvorak and Teply utilized the maximum principle for strain rates on the upper bound while the elastic minimum complementary energy theorem was used for the lower bound.

Lerch and Melis [66] predicted the stress strain response of cross-ply laminates from a micromechanical model. Residual stresses and fiber debonding were accounted for through gap elements that opened at a critical, predetermined stress state. The titanium matrix was modeled as elastic/plastic, while the fibers were assumed to remain elastic to failure. Using the MARC finite element package, good correlation of the axial and transverse stress strain behavior was found between the model and experimental results.

A three phase cylinder model, distinguishing fiber, matrix and interphase regions was utilized by Pagano and Tandon [67] to study the elastic response of multi-directional coated fiber composites. By parameterizing the mechanical properties and geometry of the interphase, the stress intensity about a thermally excited fiber was documented experimentally and numerically. Their work centered on Nicalon reinforced

BMAS, with fiber coatings composed of nickel and carbon. The derived constitutive relations were solved using the numerical package, NDSANDS.

Objective and Scope of the Investigation

The primary objective of this investigation was to develop a local-global micromechanical model for continuous fiber metal matrix composites. This finite element model is to account for energy absorbing mechanisms such as fiber debonding and matrix plasticity on a local level. Parametric studies of the interfacial bond strength and fiber volume fraction are to be presented and analyzed to provide insight on the mechanics of composite fracture. It was also intended that fracture in monolithic metals should be well understood and could be related to matrix failure in the composite model.

Chapter 2 will describe the finite element analysis procedure and will outline the various case studies. Modifications that were made to the *PAPST* code will be highlighted along with various post processors used to analyze the data. Chapter 3 will discuss the computational results of both the two dimensional elastic-plastic fracture problems as well as the local-global composite fracture problem. Chapters 4 and 5 will present important conclusions and give recommendations for future work, respectively.

CHAPTER 2

NUMERICAL PROCEDURE

To study the fracture characteristics of metal matrix composites, a two part investigation was necessary. First a detailed, nonlinear finite element analysis has been carried out on a variety of structural alloys. The numerical code, *PAPST* [68], was modified to perform the present analysis. Furthermore, a local-global investigation has been conducted using the commercially available package, *ANSYS*.

Fracture of Monolithic Metals

Listed below are the capabilities and modifications that have been made to the *PAPST* code. The execution procedure and additional postprocessors have been documented to account for all the changes.

Capabilities of *PAPST*

PAPST (Plastic Axisymmetric/Planar Structures) can be traced back to another finite element code, *APES*, which was limited to linear elastic fracture problems [69,70]. Gifford and Nash subsequently modified this code to accept nonlinear material characteristics and have published their findings on crack problems in elastic-plastic materials [71]. To handle the mathematical instability at the crack tip, a special enriched mode I singularity element was incorporated with 8x8 Gaussian quadrature.

Away from the highly stressed regions, *PAPST* uses 12-noded isoparametric quadrilateral 2-D elements with 4x4 Gaussian quadrature. All of the nodes are located on the perimeter of the element. These elements allow stresses to vary over the face of the element thus requiring fewer elements to model a given structure. Both element types are capable of handling linear hardening materials such as those studied by Hutchinson [30], Rice and Rosengren [31]. A comparison to constant stress (strain) triangular elements is given in the *APES* manual [69,70] showing the accuracy of using these enhanced elements.

Solutions are obtained nonlinearly using the Newton-Raphson iteration technique [72]. The nonlinear capability of *PAPST* incorporates the J_2 -incremental flow theory of plasticity and the Von Mises yield criteria. The incremental plasticity theory is given as [68]:

$$\dot{e}_{ij} = \frac{1 + \nu}{E} \dot{s}_{ij} + \frac{3}{2} f(\sigma_e) s'_{ij} \sigma'_e \quad \text{for } \sigma'_e = \sigma_{yd, \text{current}} \text{ and } \sigma'_e > 0 \quad (2.1)$$

$$\dot{e}_{ij} = \frac{1 + \nu}{E} \dot{s}_{ij} \quad (\text{otherwise}) \quad (2.2)$$

where σ_e is the effective stress and σ'_e is the Von Mises effective stress with respect to the coordinates of the current center of the yield surface. *PAPST* approximates the true stress-strain curve of a material using either multilinear or Ramberg-Osgood power hardening approximations. *PAPST* is capable of modeling either purely kinematic or isotropic hardening materials or may model a mixture of the two. Kinematic hardening is when the center of the yield surface is found to move, while isotropic hardening is when the yield surface expands uniformly. *PAPST* handles both plane stress and plane

strain conditions. The *J*-Integral, an important parameter in nonlinear fracture mechanics, may be calculated over 10 paths surrounding the crack tip.

Modifications Made to *PAPST*

The *PAPST* code has been in existence in some form or another since 1972. In 1984 this code was modified to run on the VAX mainframe environment by Bhagat et al. [73]. The code was subsequently termed *ARLPAPST* which was substantially expanded in its solution capability and integrated pre- and postprocessing subroutines. *ARLPAPST* handled, at most, 50 elements or 500 nodes as was the case with *PAPST*. The original intent of this thesis was to model composite materials using *ARLPAPST*; therefore the code was altered to handle an order of magnitude greater number of elements and nodes.

Several arrays including those controlling boundary conditions, thermal effects, spring elements and global solution matrices were altered in size. From personal communications with Gifford [68], the following formula was used to determine the array size of *G*, the global solution matrix, where *N* is the number of nodes:

$$G = 2 \cdot (N + 1)^2 \quad (2.3)$$

Additional Postprocessors

Modifications were made to output the strain energy density, selected *J*-Integral values and plots of the deformed mesh. To analyze crack instability, values of the strain energy density (*dW/dV*) were required. Since *ARLPAPST* generates *dW/dV* when

calculating J , a write statement placed in the code outputs dW/dV without additional effort. This write statement was designed to only print out dW/dV along the first J -Integral path to save disk space. The nodes along the path do not need to form a closed contour. The post processors that were written to cut J and generate postscript output of the deformed structure are listed in appendices A and B respectively. Finally, contour plots were generated using SAS graph on IBM 3179 terminals and pen plotters.

Solution Procedure

The solution procedure for analyzing nonlinear elastoplastic fracture problems with *ARLPAPST* is outlined in Fig. 2.1.

Materials Under Investigation

Two types of steel (HY-130 and HY-140) as well as two types of aluminum alloys (7075 and 5083-O) have been investigated. The compact tension specimens that have been analyzed conform to current ASTM standards, see Table 2.1. Multilinear material modeling of the true stress strain curves are used to represent all the materials as is shown in Fig. 2.2. Typical mesh designs are presented in Chapter 3 (refer to Figs. 3.1 and 3.2).

Local-Global Micromechanical Modeling

The second stage of this investigation centered on the fracture behavior of SCS-6/Ti-15-3 composite. Johnson et al. [48] performed exhaustive experimental work on

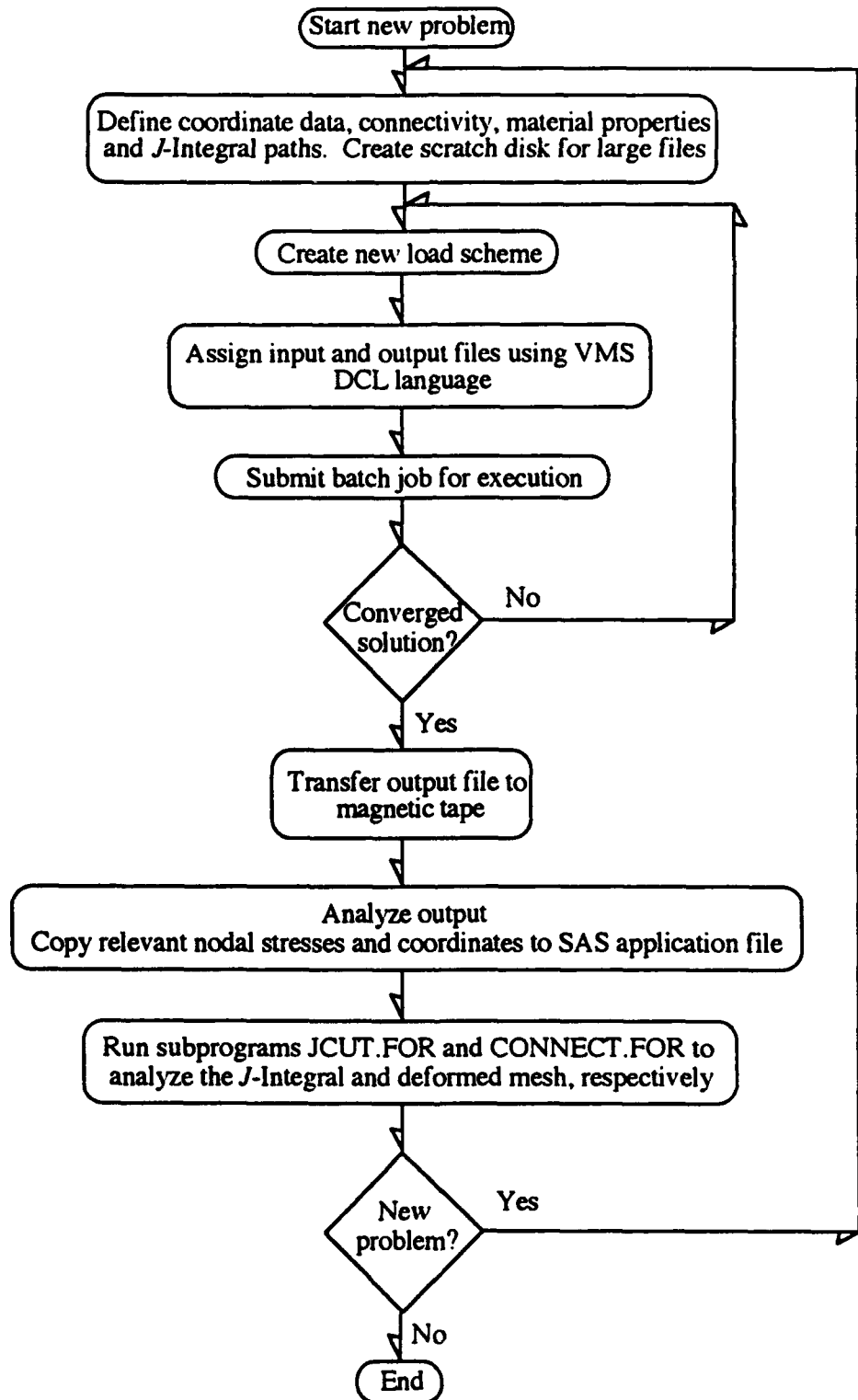


Figure 2.1. Flowchart for analyzing elastic-plastic fracture problems using the modified ARLPAPST finite element code

Table 2.1. Compact tension specimen geometry and material data

Material	W (mm)	B (mm)	a (mm)	a/W	σ_y (MPa)	Condition	Reference
HY-130	50.8	25.4	39.04	0.7685	896.3	plane ε	[71]
	50.8	25.4	41.22	0.8115			
	50.8	25.4	42.92	0.8843			
	50.8	25.4	25.40	0.5000			
HY-140	50.8	25.4	39.04	0.7685	965.3	plane ε	[71]
7075 Al	50.8	25.4	39.04	0.7685	413.7	plane ε	[74]
	50.8	25.4	41.22	0.8115			
5083-O Al	152.4	45.7	81.28	0.5333	121.8	plane σ	[75]
	152.4	45.7	81.28	0.5333	121.9	plane ε	

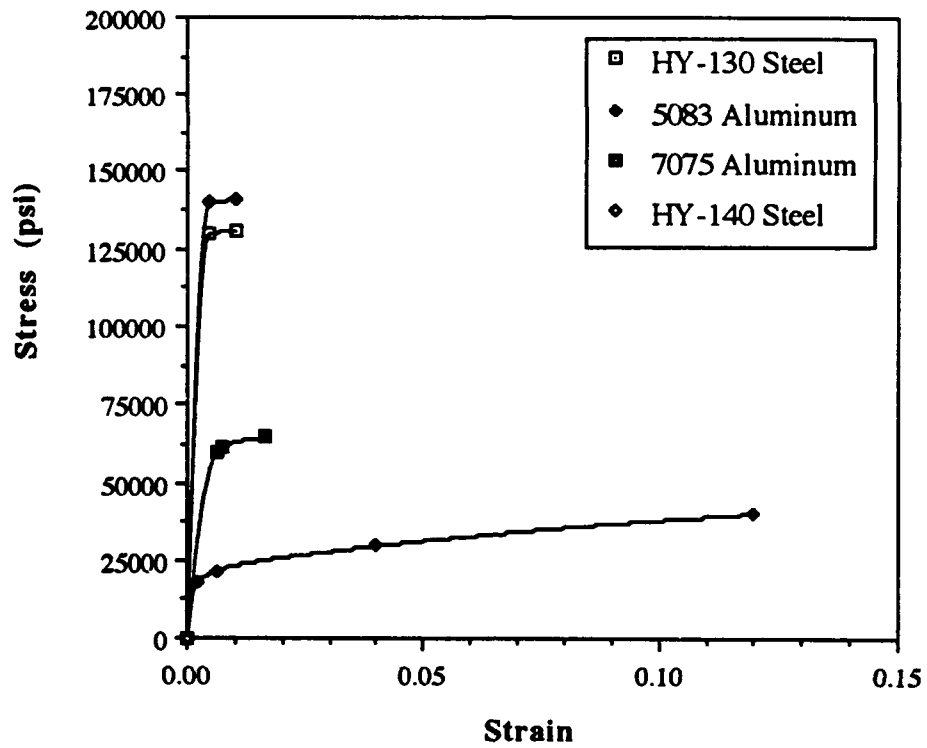


Figure 2.2. True stress-strain curves of HY-130 steel, HY-140 steel and 5083-O aluminum and 7075 aluminum.

this material, characterizing the stress strain behavior of multi-ply systems. Their work indicates that SCS-6/Ti-15-3 possesses a weak interface (138 MPa) which they have documented. Lerch and Melis [66] have used their work to model cross-ply composites and consider the work of Johnson et al. [48] to be comprehensive.

Material Properties

The compiled properties of silicon carbide SCS-6 fibers, as fabricated Ti-15V-3Cr-3Al-3Sn and unidirectional as fabricated SCS-6/Ti-15-3 composite are listed in Table 2.2. The nonlinear stress-strain data used for the local model is presented in Fig. 2.3. Only the elastic properties of the composite are used on the global level.

Numerical Approach

First a global elastic analysis was performed on composite using specimen dimensions extracted from the work of Johnson et al. [48]. The center cracked plate under study was modeled using the boundary conditions shown in Fig. 2.4. A fully three dimensional global analysis was not performed due to a lack of experimental data of the necessary five independent elastic constants. Instead a two-dimensional, plane strain model, which incorporates three independent elastic constants, was studied with orthotropic elements (STIF 82) using the ANSYS finite element code. A uniform displacement of $2.5 \mu\text{m}$ was applied to the top edge of the model, corresponding to the minimum displacement necessary to induce a transverse stress greater than 138 MPa, the stress at which fiber debonding occurs. Four finite element meshes with varying number of elements were then analyzed to optimize the numerical solution. A sample input file is presented in Appendix C. The results of this optimization will be presented

Table 2.2. Compiled properties of fiber, matrix and composite for SCS-6/Ti-15-3 system (properties extracted from reference 48).

Properties of the fiber		
Coefficient of Thermal Expansion (α)	$2.70 \times 10^{-6} \text{ }^{\circ}\text{F}^{-1}$	$4.09 \times 10^{-6} \text{ }^{\circ}\text{C}^{-1}$
Poisson's Ratio (ν)	0.25	0.25
Fiber Diameter (d)	0.0056 in	0.014224 cm
Longitudinal Elastic Modulus	$58.0 \times 10^6 \text{ psi}$	399.9 GPa
Transverse Elastic Modulus	$58.0 \times 10^6 \text{ psi}$	399.9 GPa
Ultimate Strength	$465 \times 10^3 \text{ psi}$	3208 MPa
Properties of the matrix (as fabricated)		
Coefficient of Thermal Expansion (α)	$5.4 \times 10^{-6} \text{ }^{\circ}\text{F}^{-1}$	$9.72 \times 10^{-6} \text{ }^{\circ}\text{C}^{-1}$
Poisson's Ratio (ν)	0.351	0.351
Longitudinal Elastic Modulus	$13.4 \times 10^6 \text{ psi}$	92.39 GPa
Yield Stress	$100.0 \times 10^3 \text{ psi}$	689.5 MPa
Ultimate Stress	$135.4 \times 10^3 \text{ psi}$	933.55 MPa
Properties of the composite (as fabricated [0] _g laminate)		
Fiber Volume Fraction	0.325	0.325
Poisson's Ratio (ν)	0.299	0.299
Debond Stress	$20 \times 10^3 \text{ psi}$	138 MPa
Ultimate Strength	$220 \times 10^3 \text{ psi}$	1518 MPa

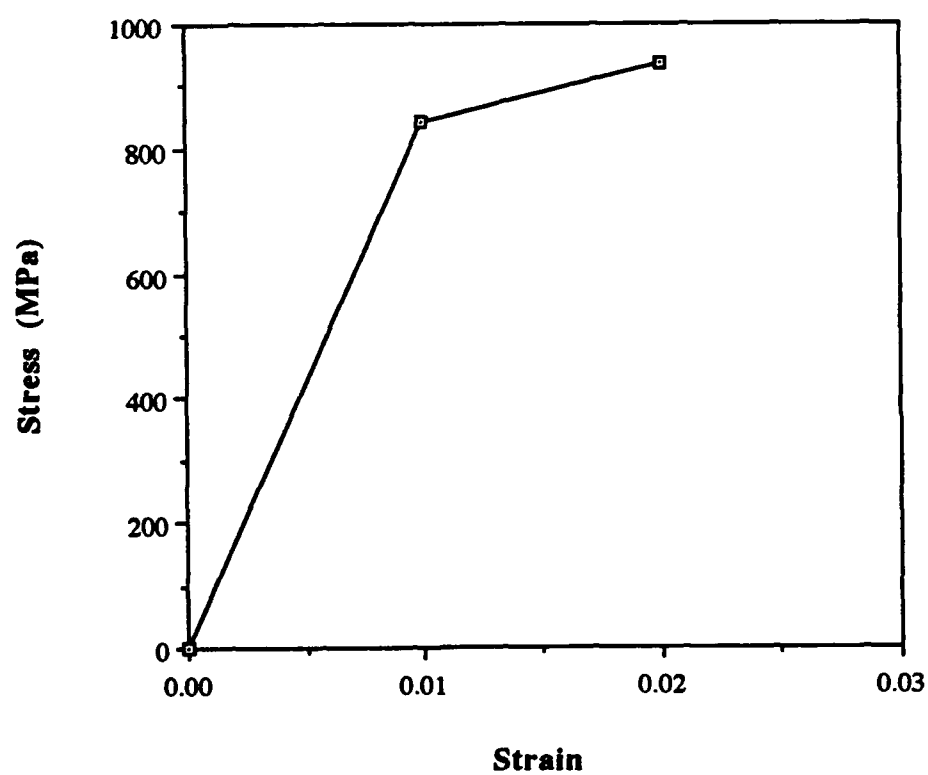


Figure 2.3. Nonlinear stress-strain curve used to model titanium 15-3 matrix material on the local level.

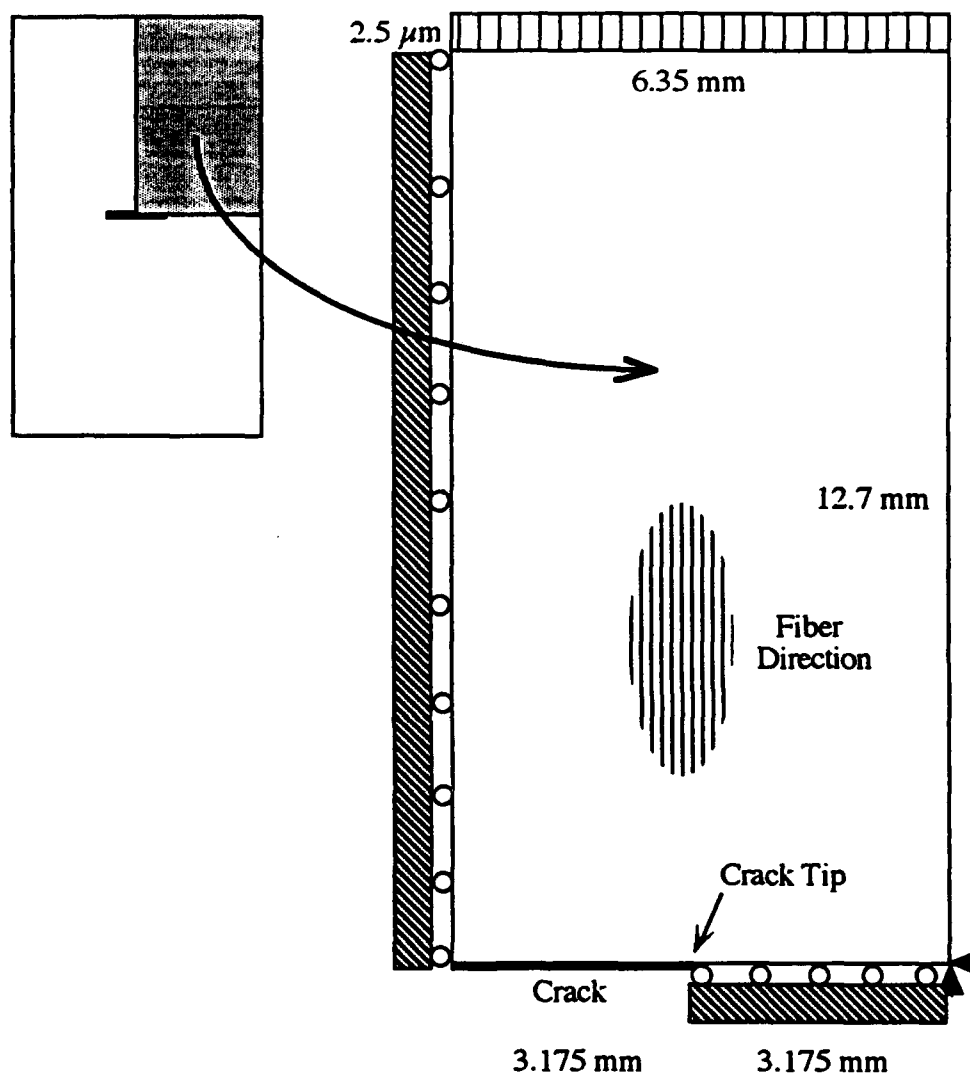


Figure 2.4. Schematic of the macroscopic model showing boundary conditions, fiber orientation and specimen dimensions.

in Chapter 3. The displacements in the most highly stressed region of the optimized model were then used as the boundary conditions for the local model.

The three-dimensional local model discretizes the fiber, matrix and interphase into a unit cell after the work of Dvorak and Teply [61]. A representative unit cell with a volume fraction of 0.325 is shown in Fig. 2.5. Equation 2.4 enables the calculation of the interfiber spacing (λ) of the unit cell model.

$$\lambda = 2r \left[0.5373 \sqrt{\frac{\pi}{V_f}} \right] \quad (2.4)$$

The fiber and matrix regions were constructed with 20-noded isoparametric elements (STIF 95) using the ANSYS finite element code, while gap elements were placed along the fiber-matrix interface.

A parametric study of the interface strength was performed by varying the fiber-matrix debond stress. The tensile strength of the interface, σ_i , was set equal to 138 MPa, corresponding to the experimentally determined debond stress [48]. As an extreme case, σ_i was equated to σ_f , the fiber strength. From the initial analysis this gave unreasonable results and an intermediate value was chosen, corresponding to the strength of the matrix. The stiffness of the gap element is assumed to be equal to that of the matrix (92.4 MPa). Various interface strengths are incorporated through changes in radial interference (with units of displacement). To calculate the radial strain seen by the gap elements and the surrounding material, the effective length acting on an individual element is assumed to be of length 0.5λ (see equation 2.4). Thus the interface strength is modeled as an effective strain acting upon the fiber-matrix interface. Another effective length may or may not be appropriate, but this length seems to be reasonable. Using Hooke's law, the desired interface strength is divided by the gap stiffness to obtain the

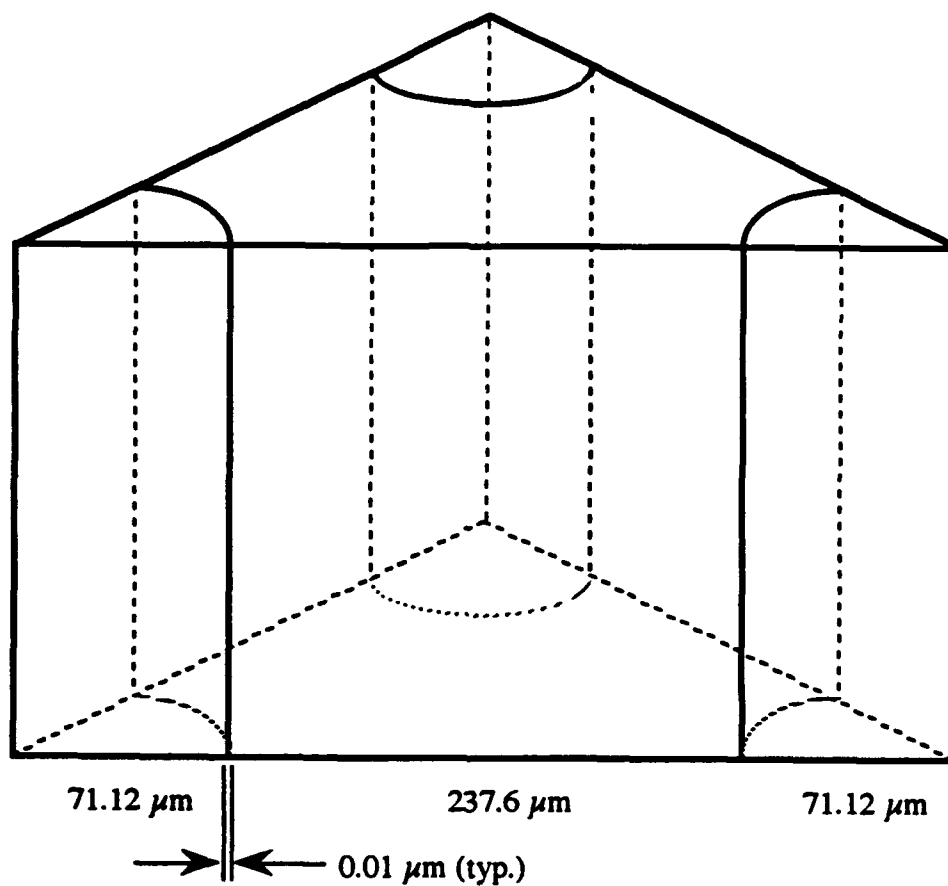
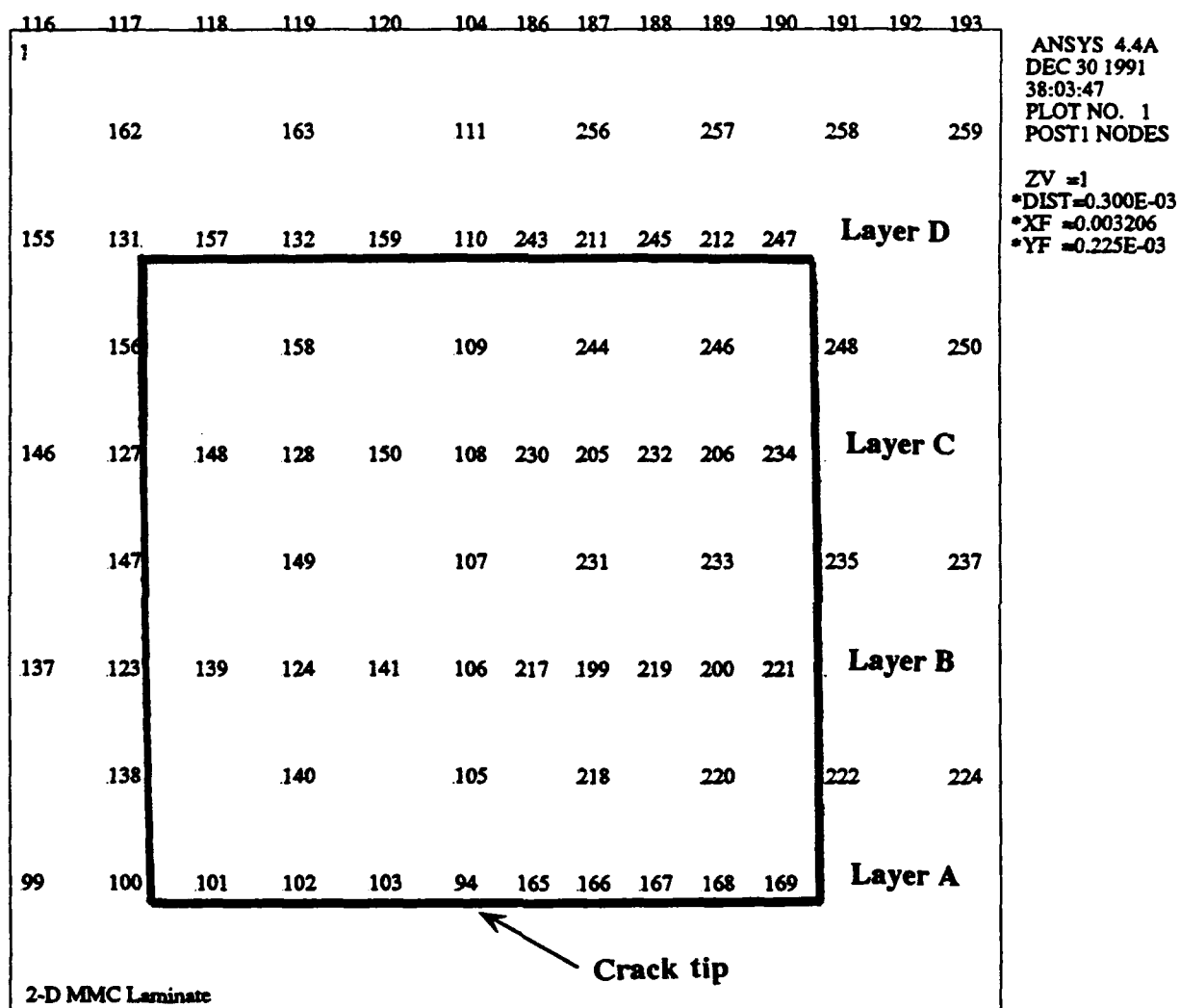


Figure 2.5. Representative unit cell distinguishing fiber, matrix and interphase of a 0.325 volume fraction SiC/Ti composite. The fiber is modeled as elastic, while the matrix is elastoplastic. Gap elements are used to simulate the interfacial region.

gap strain. These strain values are multiplied by the factor 0.5λ to obtain the interference length. For model continuity, a small mathematical separation ($0.01\ \mu\text{m}$) is placed between the two nodes of the gap element.

The pictorial shown in Fig 2.6 emphasizes how the boundary conditions of the global model are transferred to the local model. Part A of Fig. 2.6 represents the entire specimen modeled by Johnson et al. [48]. Through the use of symmetry conditions, part B of Fig. 2.6 was used as the global or "macro" model. The horizontal and vertical displacements were extracted from the nodes of the global model corresponding to the top and bottom layers of the local model as shown in part C of Fig. 2.6. The height of the microscopic model ($380.0\ \mu\text{m}$) corresponds to approximately four layers of "macro-model" nodes as shown in Fig. 2.7. These displacements were plotted and fit with a polynomial curve. The fitted curves and corresponding displacements will be presented in the following chapter. When the R^2 correlation of the data points was less than 0.92, then visual interpolation from the graphs was used. The fitted displacement boundary conditions were then transferred to the 3-dimensional local model via coordinate transformation as is shown in part D of Fig. 2.6. The (x', y', z') axes denote the coordinate system used to construct the local model. The (X, Y, Z) axes denote the coordinate system of the global model. The displacements along the global Z direction are assumed to remain unchanged.



CHAPTER 3

RESULTS AND DISCUSSION

The objective of our research is divided into two separate stages. First, a detailed analysis of elastic-plastic fracture in unreinforced metals is conducted, followed by a study of the micromechanics of fracture in silicon carbide reinforced titanium. The study of monolithic steel and aluminum alloys gave the opportunity to verify work that has been performed in the past as well as serve as a benchmark for problems solved using the updated version of *ARLPAPST*.

Monolithic Materials

Due to the ductile nature of steel and aluminum we were interested in the crack tip plastic zone (CTPZ) and its dependence on the crack length. J -Integral values were established on several different paths in both steel and aluminum specimens and the relative path independence of J will be defended. The strain energy parameters $(dW/dV)_c$ and $(dW/dV)_{min}$ presented by Bhagat et al. [72] were verified and will be discussed at length. Finally, stress and strain contour plots are presented to study how the stresses are distributed in front of the crack tip.

Mesh Deformation

Plots of the deformed meshes of 5083-O aluminum and 7075 aluminum are given in Figs. 3.1 and 3.2, respectively. The deformed mesh shown in Fig. 3.1 corresponds to an applied load of 6122.5 pounds, while that in Fig. 3.2 corresponds to an applied load of 2844 pounds. The J -Integral paths are located as shown. These loads represent the crack initiation loads. In the next section, the crack initiation load will be described in terms of the strain energy density.

Strain Energy Density

The strain energy density (dW/dV) in front of the crack tip as described by Sih [39,40] was calculated using *ARLPAPST*. At a critical radius r_c , the strain energy density dropped to a minimum value designated $(dW/dV)_{min}$ as is shown in Figs. 3.3 and 3.4. Earlier studies have shown that this "U-shaped" signature is found only in the $\Theta=0^\circ$ direction ahead of the crack tip [72]. Note that in Fig. 3.4 the strain energy density exhibits a jagged signature. This corresponds to unloading at the crack tip. These values of $(dW/dV)_{min}$ were plotted against the applied load and at a critical load, P^* , the values of dW/dV began to decrease as is shown in Fig. 3.5. This peak value of the strain energy density signifies the point at which the structure begins to expend energy in the form of crack growth. The maximum value of $(dW/dV)_{min}$ is denoted as $(dW/dV)^*_{min}$.

Three different crack lengths in HY-130 steel and two crack lengths in 7075 aluminum were analyzed. For the specimens in which the numerical solutions remained stable, the failure load can be approximated by extrapolating the curve down the load axis. For example, in HY-130 steel with $a=1.623$, the extrapolated curve

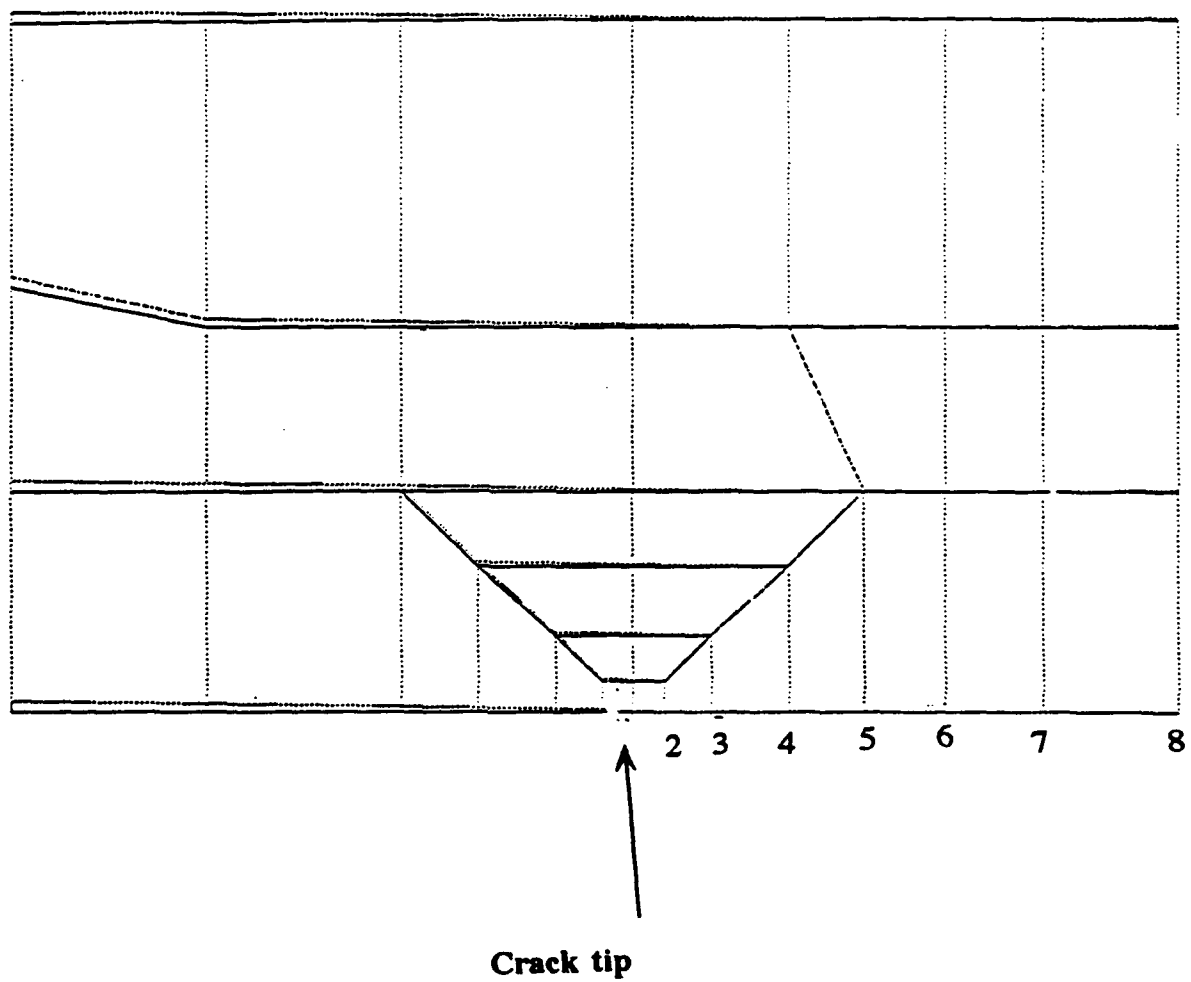


Figure 3.1. Picture showing the deformed upper half of a compact tension specimen model constructed of 5083-O aluminum. The crack tip ($a=3.199$ in) is located as shown.

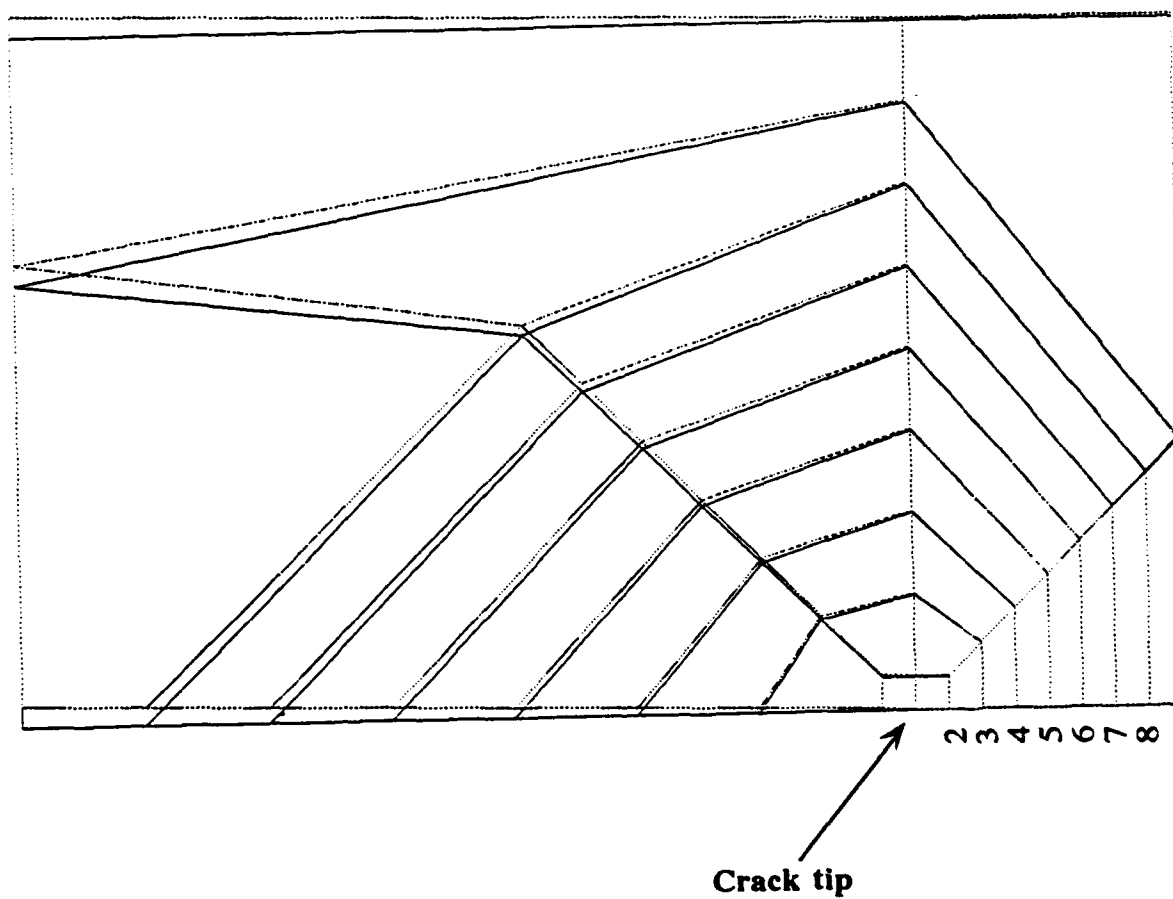


Figure 3.2. Picture showing the deformed upper half of a compact tension specimen model constructed of 7075 aluminum. The crack tip ($a=1.537$ in) is located as shown.

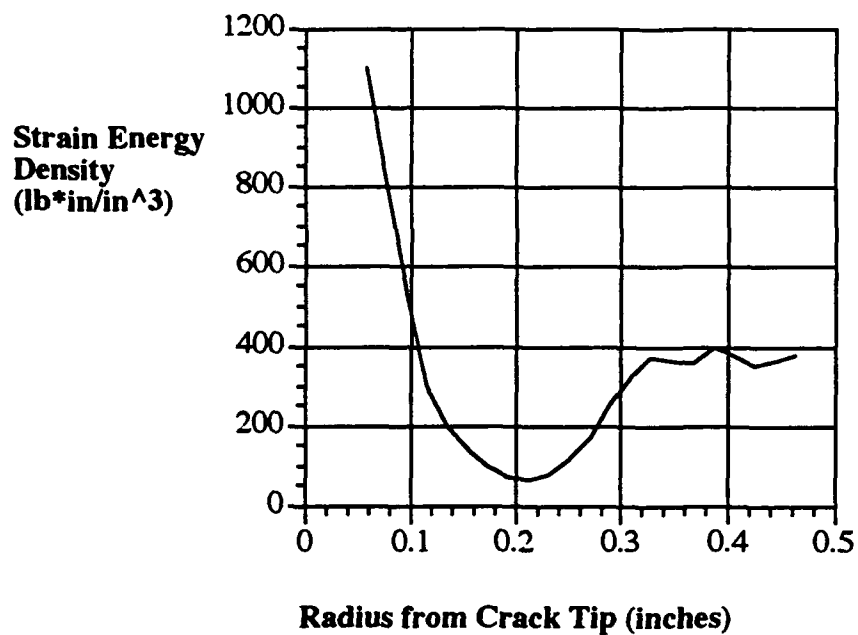


Figure 3.3. Strain energy density plotted against the radial distance from the crack tip in HY-130 steel ($a=1.537$ in).

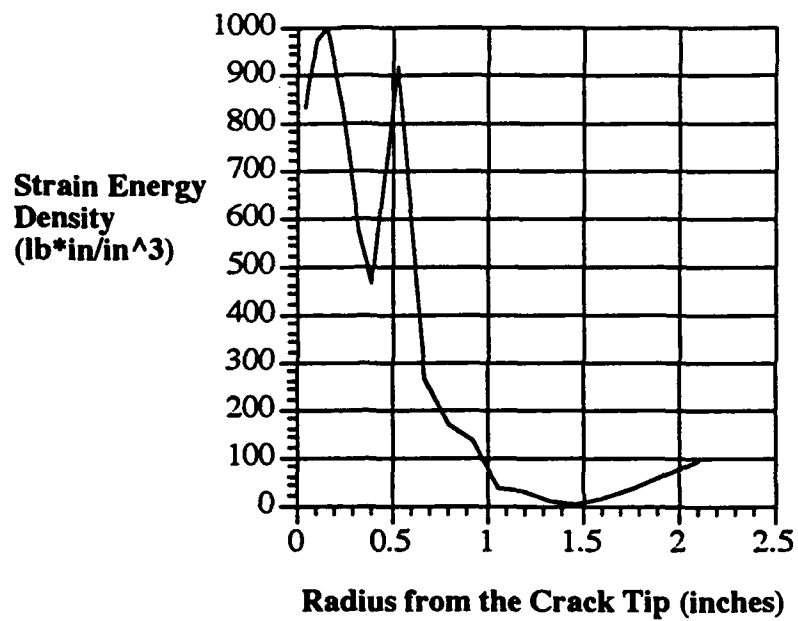


Figure 3.4. Strain energy density plotted against the radial distance from the crack tip in 5083 aluminum ($a=3.199$ in).

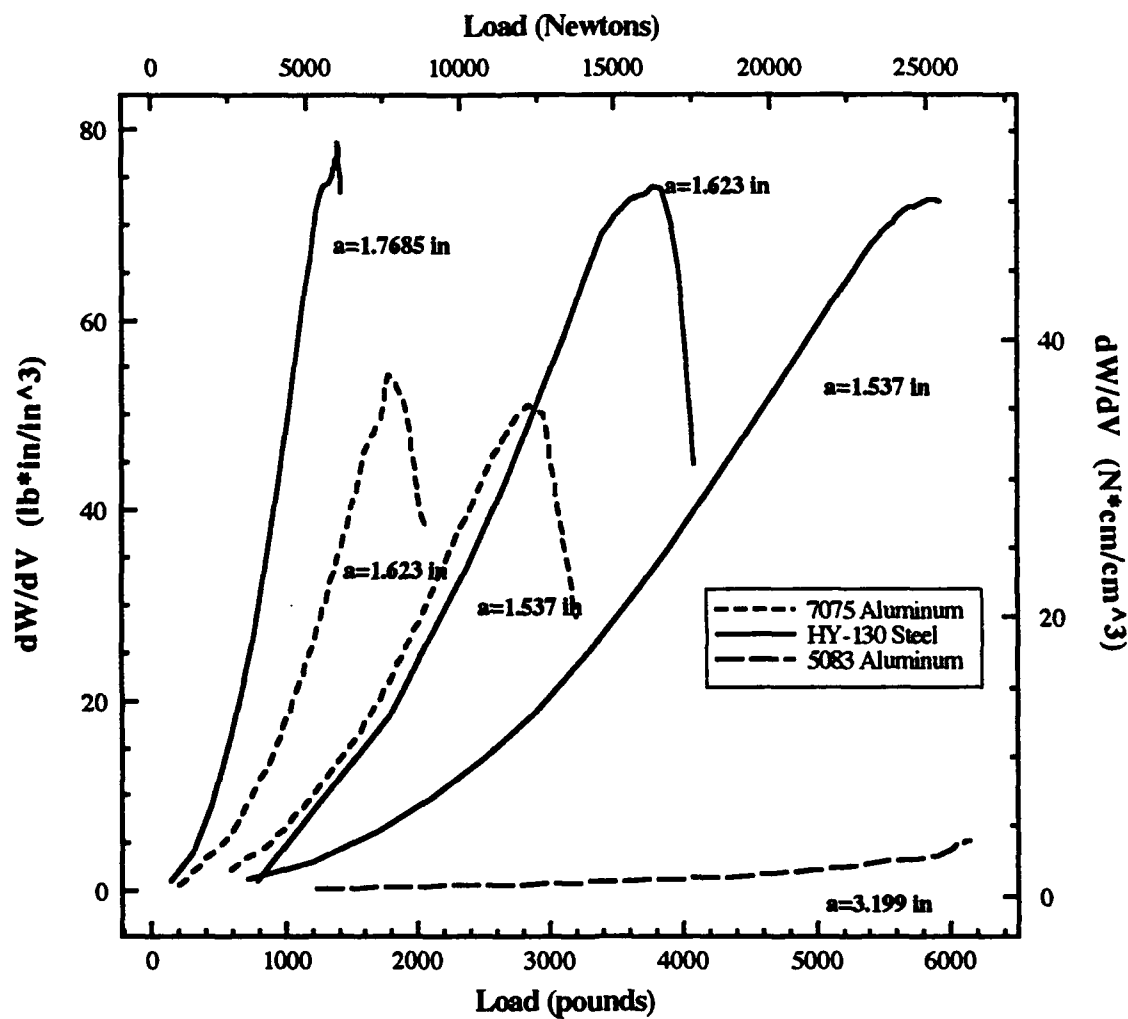


Figure 3.5. $(dW/dV)_{min}$ plotted against applied load for three crack lengths in HY-130 steel ($a=1.537$ in, 1.623 in and 1.7685 in) two crack lengths in 7075 aluminum ($a=1.537$ in and 1.623 in) and one crack length in 5083 aluminum ($a=3.199$ in). Fracture load is determined by extrapolating curve to the load axis.

reaches the load axis at 4200 pounds, and when $a=1.7623$, the predicted failure load is approximately 2100 pounds. The fracture loads of the aluminum specimens are less and the trend is similar to that observed in the steel. The fracture loads of the smaller crack lengths are consistent with fracture mechanics concepts.

Crack Tip Plasticity

The principal Von Mises stress distribution in loaded compact tension specimens of 5083 Al, 7075 Al and HY-130 steel are shown in Figs. 3.6, 3.7a, 3.7b, 3.8a, 3.8b, and 3.8c. The increasing size of the crack tip plastic zone with decreasing crack length agrees with accepted plasticity theories. For example, in Figs 3.7a and 3.7b, the ligament ahead of the crack tip for the larger crack ($a=1.623$) exhibits full plasticity for all the nodes along the ligament, while for the smaller crack ($a=1.537$) there is a small region along the ligament that remains in the elastic region.

Even though all the J contour paths in 7075 aluminum (as shown in Fig. 3.7a) pass through the CTPZ at P^* , the variation from the averaged value of J is only 3%. However, when the load is increased to $1.13P^*$ the variation from the average J value increases to 7%. Figure 3.9 illustrates how J varies along the crack ligament in 7075 aluminum ($a=1.537$) for load increments from $0.21P^*$ to $1.13P^*$. Similar trends can be observed in HY-130 and 7075 Al as shown in Figs. 3.10, 3.11 and 3.12.

The crack initiation load may be predicted by studying the variation of J as a function of applied load. Typically these plots exhibit asymptotic behavior, approaching a critical value of P . This information can then be used to predict the critical loading state of a cracked structure. The work of Hilton and Gifford [71] has been confirmed in this investigation through the plot shown in Fig 3.13.

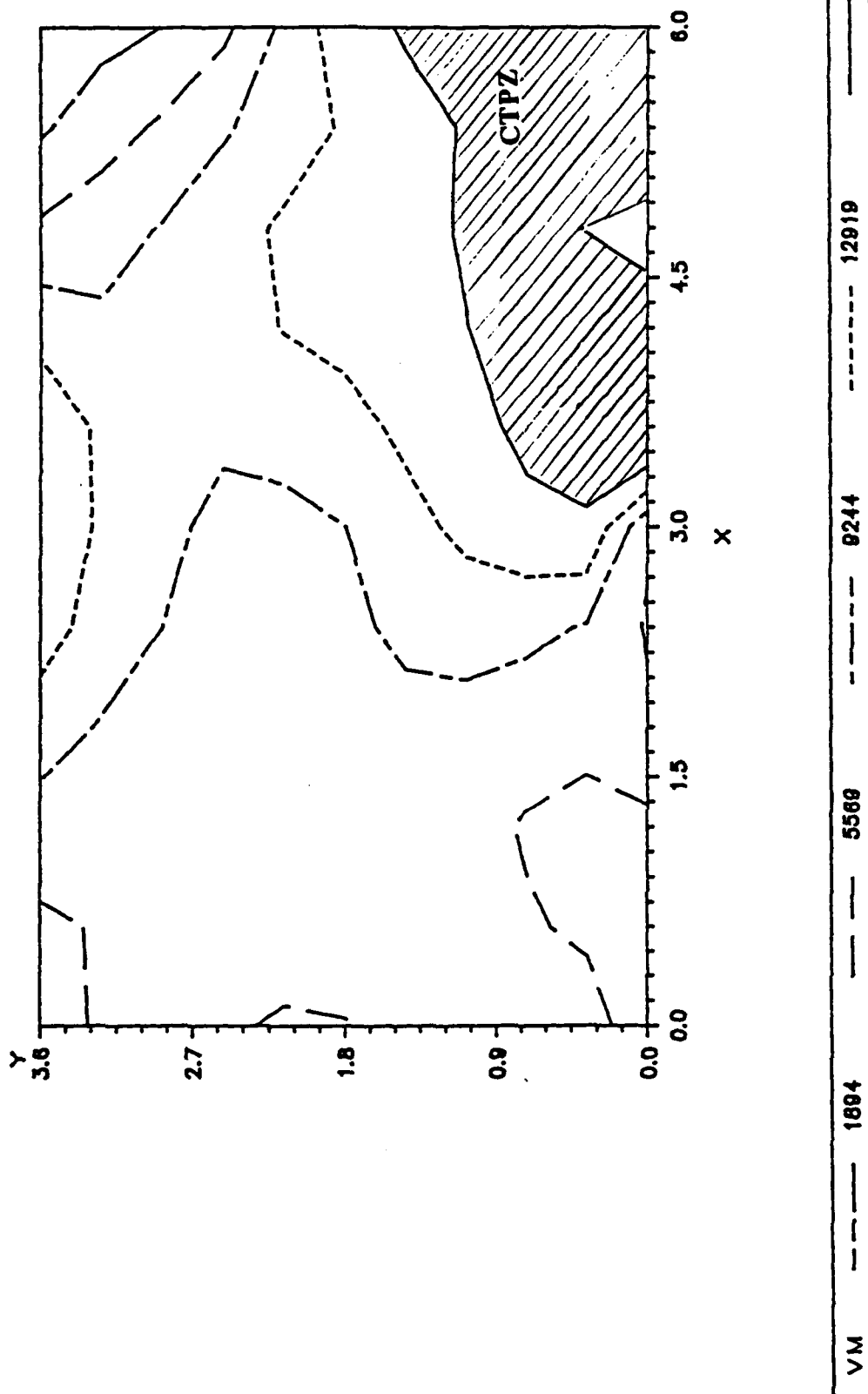


Figure 3.6. Contour plot of the Von Mises effective stress (psi) in 5083-O aluminum ($a=3.199$ in). The model is shown to scale in inches.

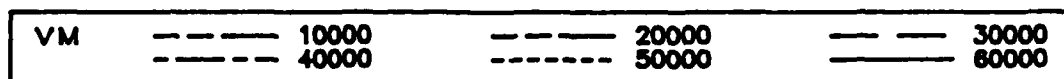
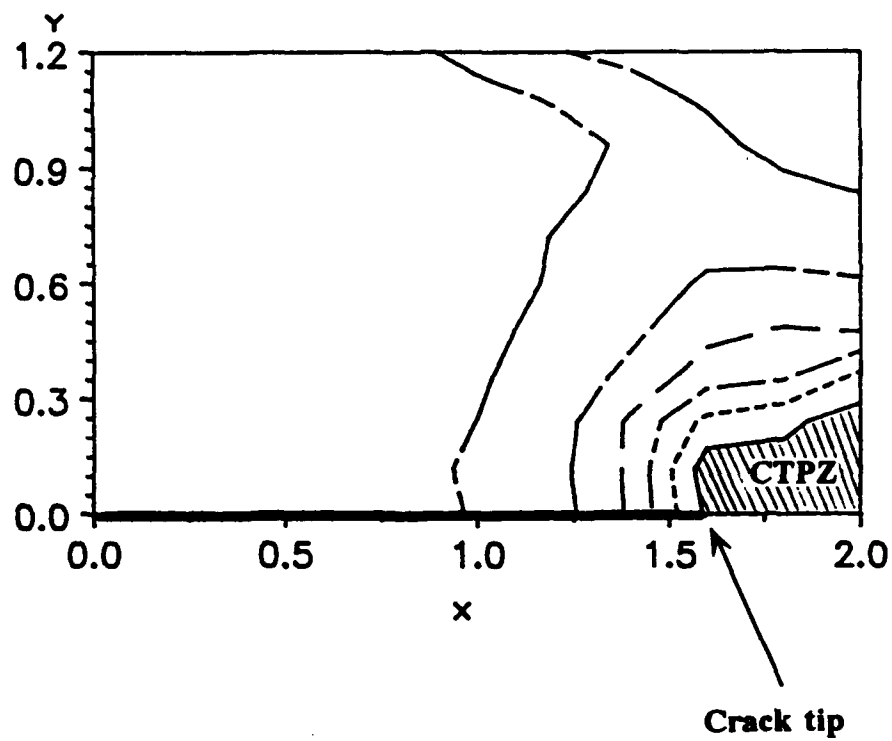


Figure 3.7a. Contour plot of the Von Mises effective stress (psi) in 7075 aluminum ($a=1.537$ in). The model is shown as 2:1 in inches.

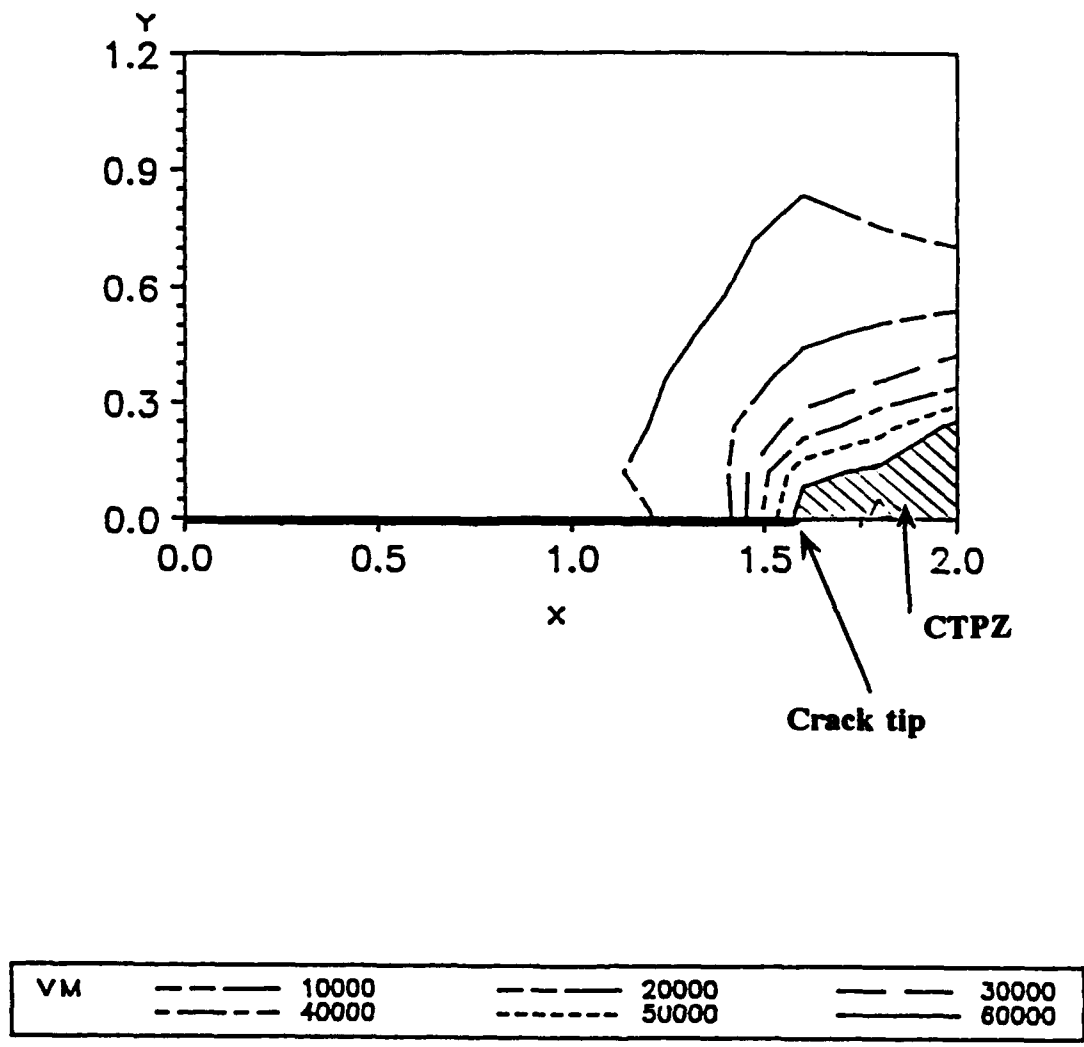
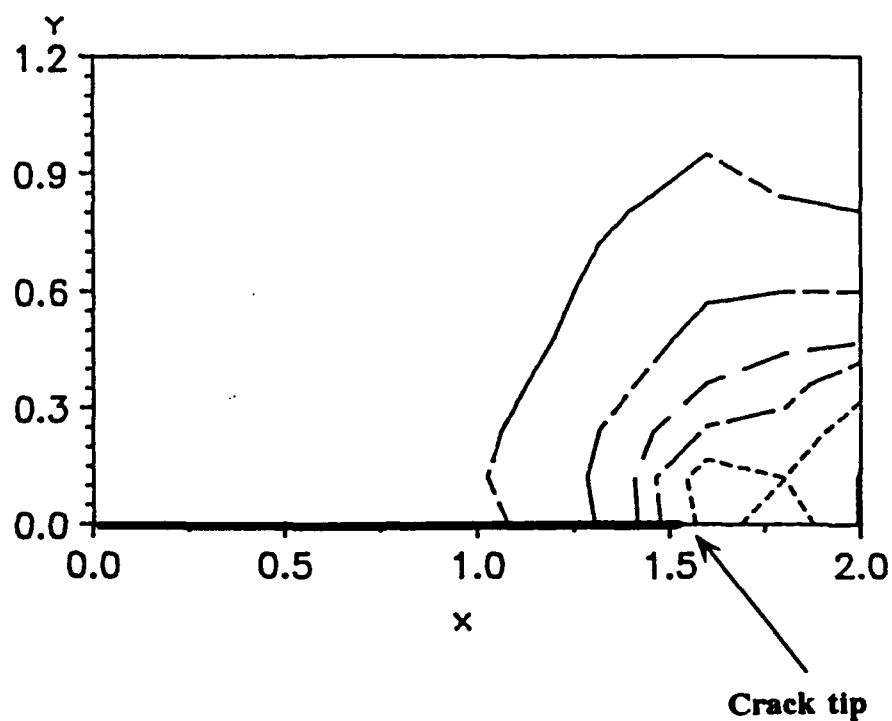
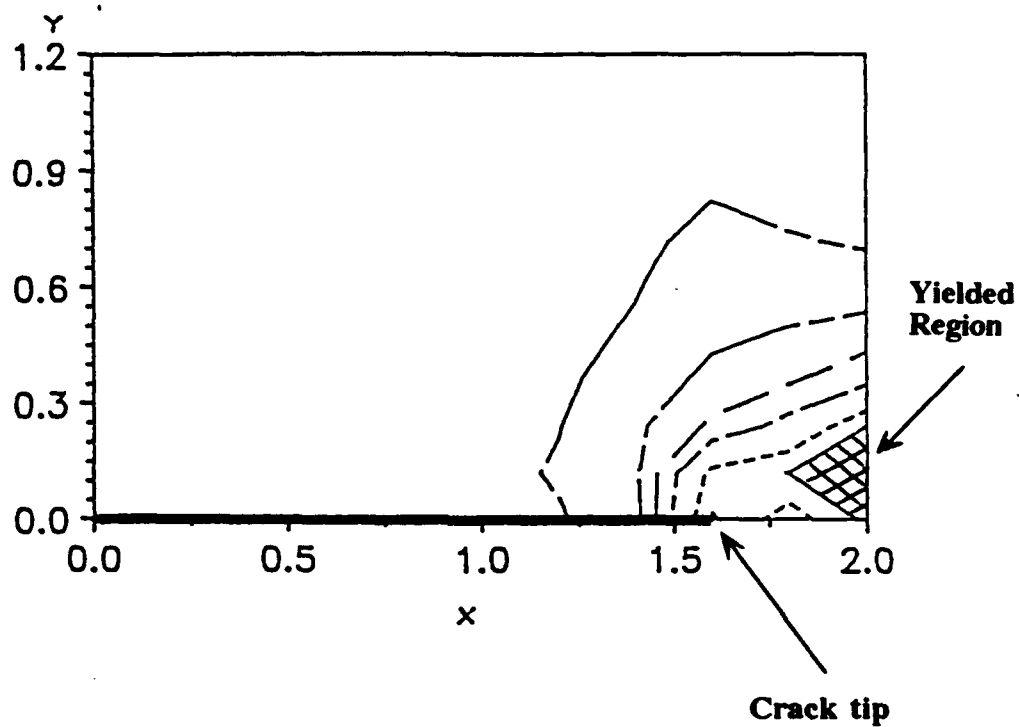


Figure 3.7b. Contour plot of the Von Mises effective stress (psi) in 7075 aluminum (a=1.623 in). The model is shown as 2:1 in inches.



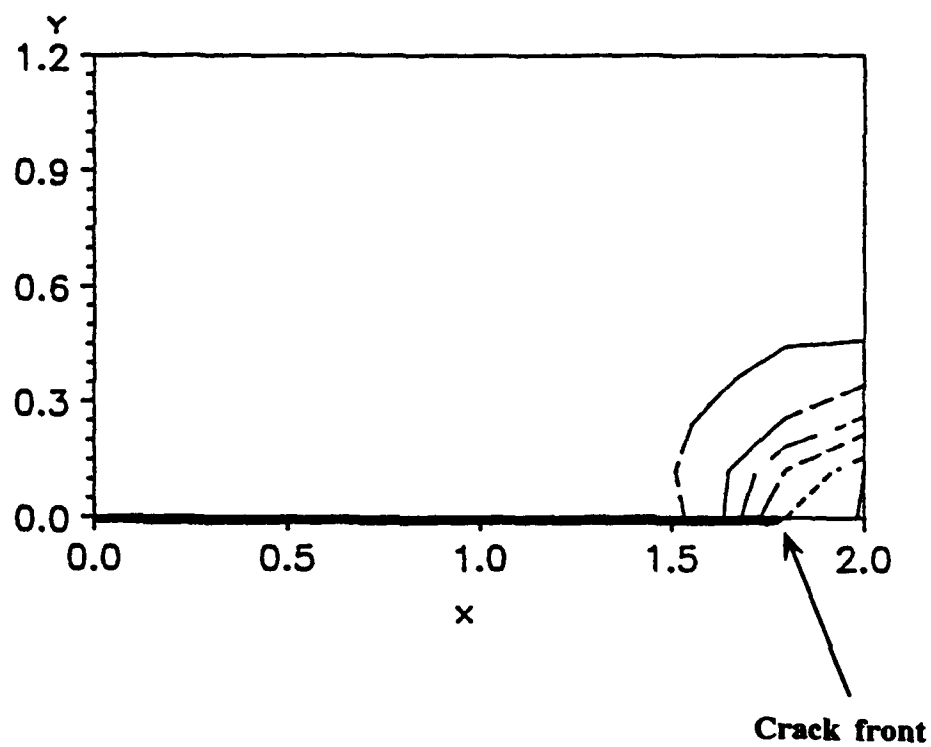
VM	-----	20000	-----	40000	-----	60000
	-----	80000	-----	110000	-----	130000

Figure 3.8a. Contour plot of the Von Mises effective stress (psi) in HY-130 steel ($a=1.537$ in). The model is shown as 2:1 in inches.



VM	-----	20000	-----	40000	-----	60000
	-----	80000	-----	110000	-----	130000

Figure 3.8b. Contour plot of the Von Mises effective stress (psi) in HY-130 steel ($a=1.623$ in). The model is shown as 2:1 in inches.



VM	-----	20000	-----	40000	-----	60000
	-----	80000	-----	110000	-----	130000

Figure 3.8c. Contour plot of the Von Mises effective stress (psi) in HY-130 steel ($a=1.7685$ in). The model is shown as 2:1 in inches.

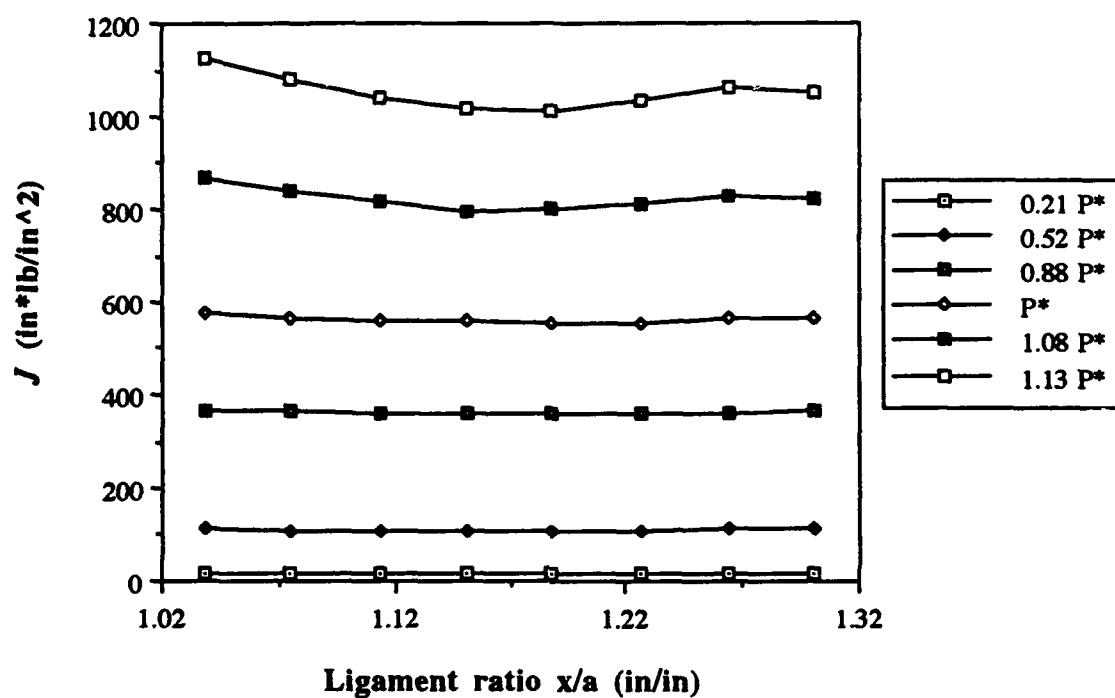


Figure 3.9. Variation of J along the crack tip ligament for 7075 aluminum ($a=1.537$ in). Note the variation of J is small until the load is increased beyond P^* . Note that $1 \text{ in*lb/in}^2 = 0.17513 \text{ kJ/m}^2$.

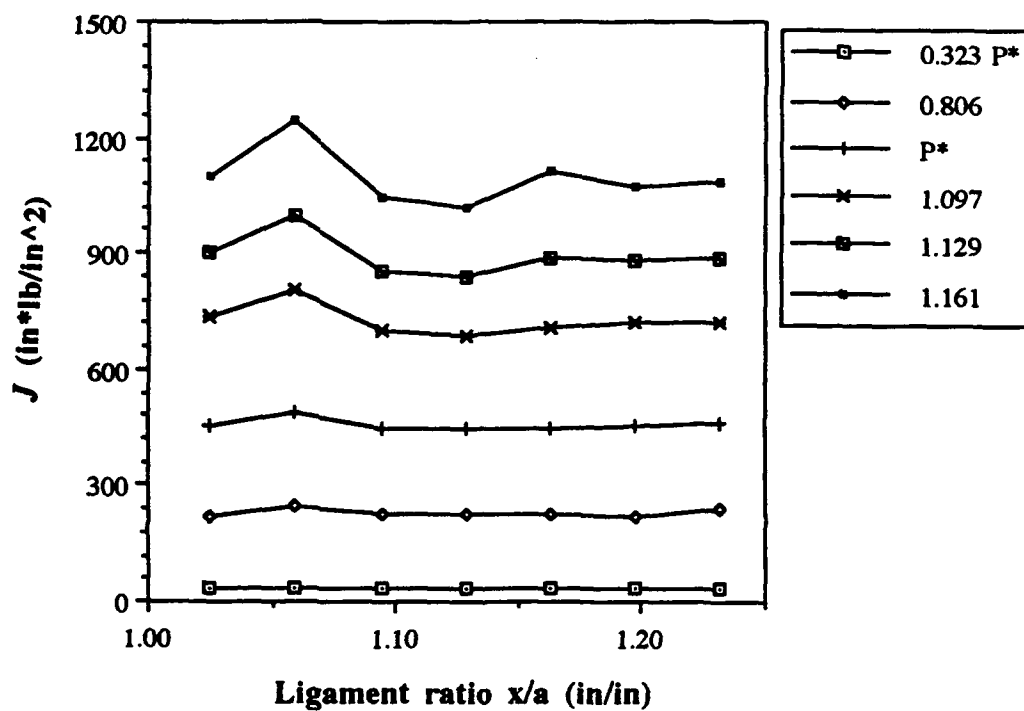


Figure. 3.10. Variation of J along the crack tip ligament for 7075 aluminum ($a=1.623$ in). Note the variation of J is small until the load is increased beyond P^* . Note that $1 \text{ in}^* \text{lb/in}^2 = 0.17513 \text{ kJ/m}^2$.

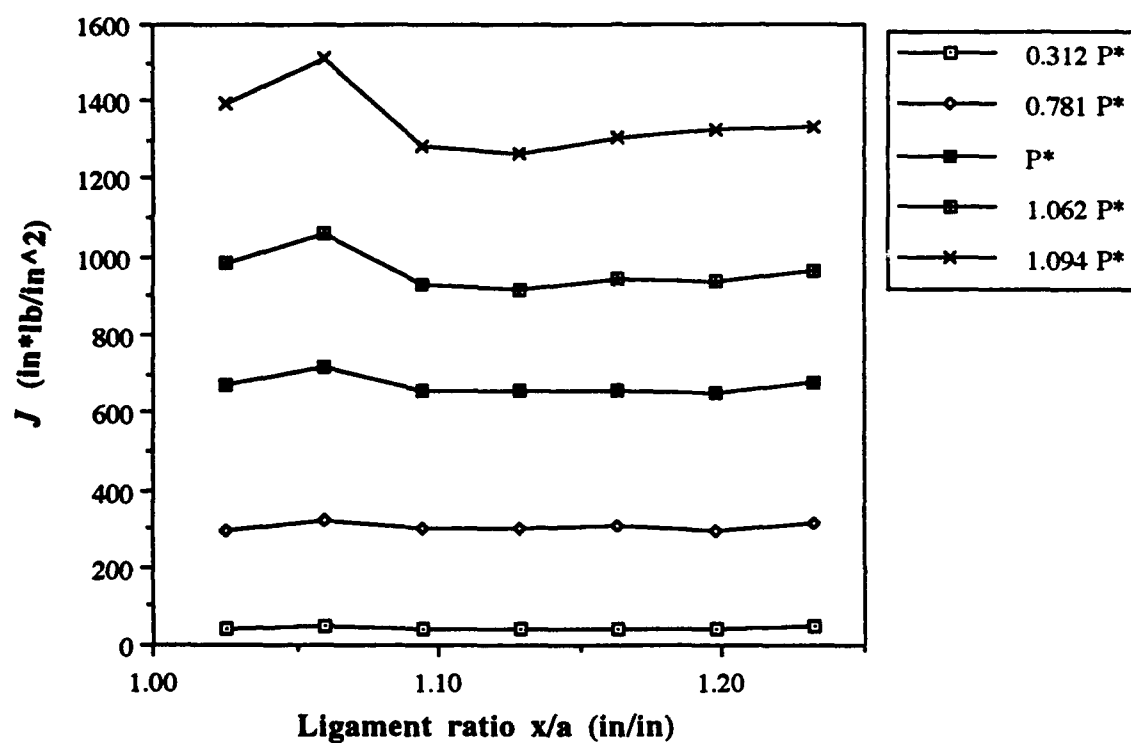


Figure 3.11. Variation of J along the crack tip ligament for HY-130 steel ($a=1.623$ in). Note the variation of J is small until the load is increased beyond P^* . Note that $1 \text{ in*lb/in}^2 = 0.17513 \text{ kJ/m}^2$.

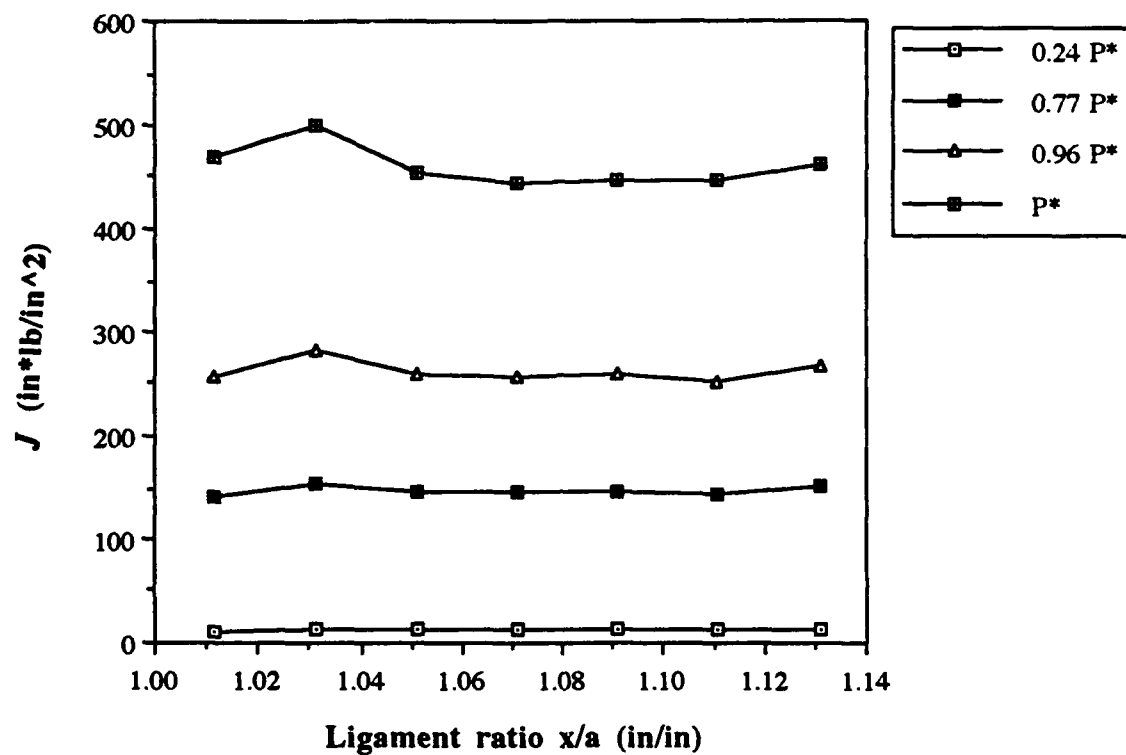


Figure 3.12. Variation of J along the crack tip ligament for HY-130 steel ($a=1.7685$ in). Note the variation of J is small until the load is increased beyond P^* . Note that $1 \text{ in*lb/in}^2 = 0.17513 \text{ kJ/m}^2$.

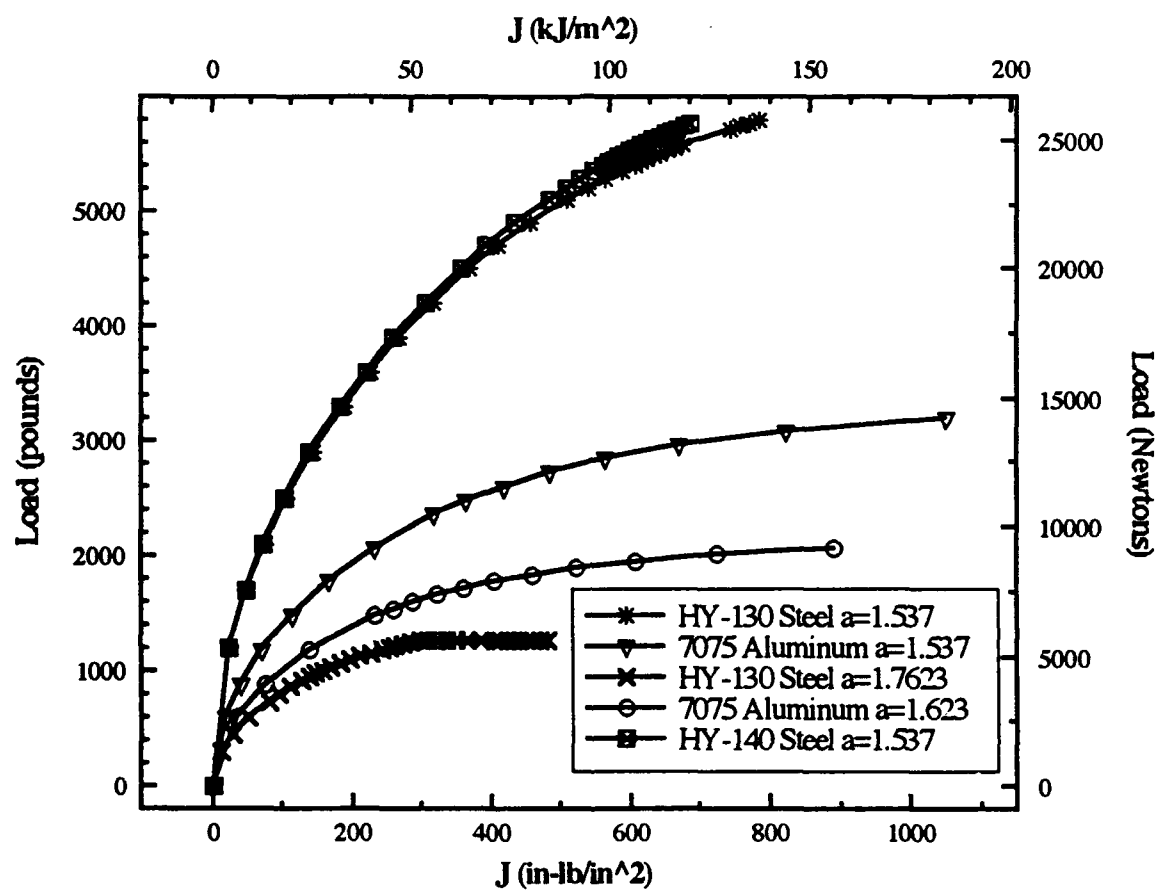


Figure 3.13. J versus applied load for aluminum and structural steel alloys.

Metal Matrix Composites

SCS-6/Ti-15-3, was chosen as our model system due to the technological significance and substantial amount of published experimental work on this material [48]. The goal in this segment of our investigation was to document the mechanics of failure under various interface strengths. As discussed earlier in Chapter 1, certain failure criteria will be documented and utilized to determine the direction and occurrence of material failure. The local-global analysis of SCS-6/Ti 15-3 was studied using the ANSYS finite element package.

Macro-Mechanics Analysis

In the analysis of orthotropic materials, an optimized mesh design is essential, even more so than in the well documented cases of steel and aluminum. Four mesh designs with 126 to 456 elements were loaded with identical boundary conditions as was described in Chapter 2. In each case, the effective principal stress at a specified node ($r = 3.74$ mm, $\theta = 8.1^\circ$) was plotted as a function of the number of elements within the mesh (see Fig. 3.14). This point is far enough away from the crack tip to provide a stable solution. As a further check, the contour plots of the principal stresses were recorded for the two meshes with the highest number of elements (refer to Figs. 3.15 and 3.16). Note that the 255 element model gives drastically different results from that of the 456 element model. Only the results from the 456 element mesh design were used in the boundary condition calculations

To accurately model the experimentally observed failure mechanisms, a combination of failure criteria must be monitored. The initial mechanisms include fiber pull-out and matrix plasticity. When loads are further increased, the fiber or matrix may

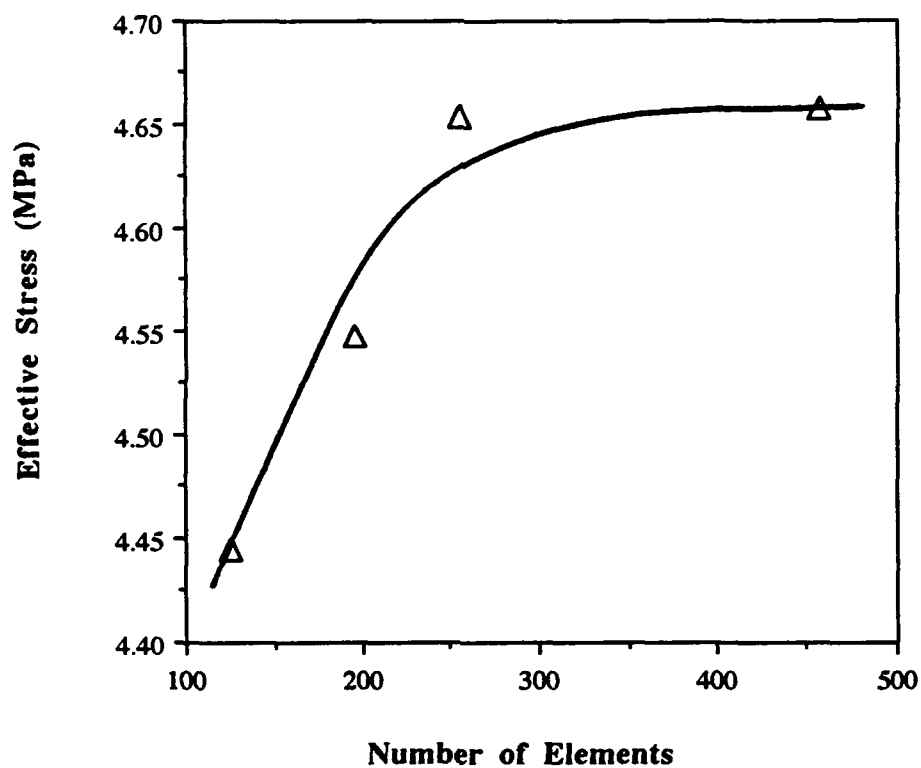


Figure 3.14. Optimization of finite element mesh for global model considering the effective stress at a radius of 3.74 mm away from the crack tip. The material system is SCS-6/Ti-15-3.

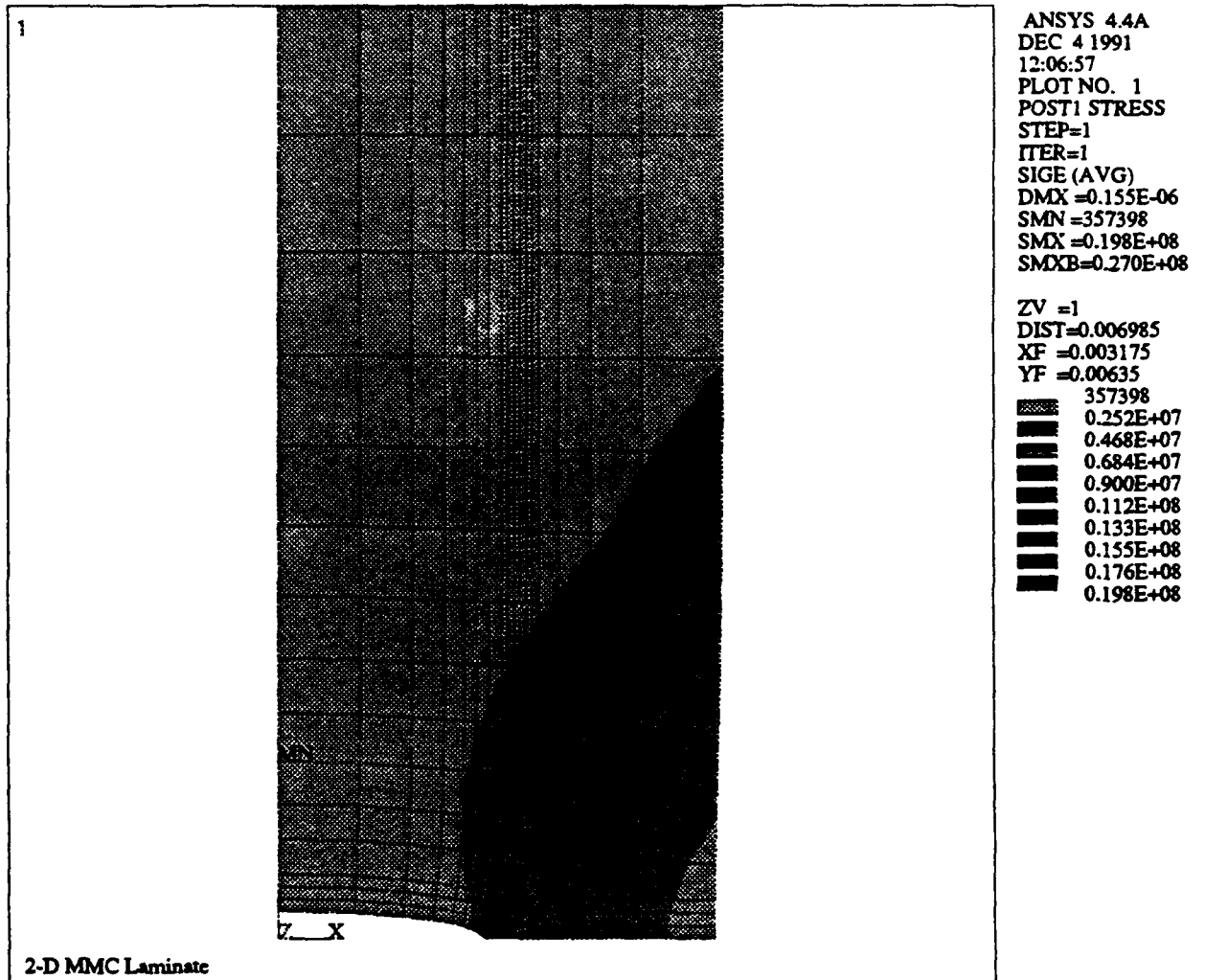


Figure 3.15. Effective stress contour plot in 255 element macroscopic model. The plate is modeled using quarter symmetry, the crack tip is located in the lower left corner.

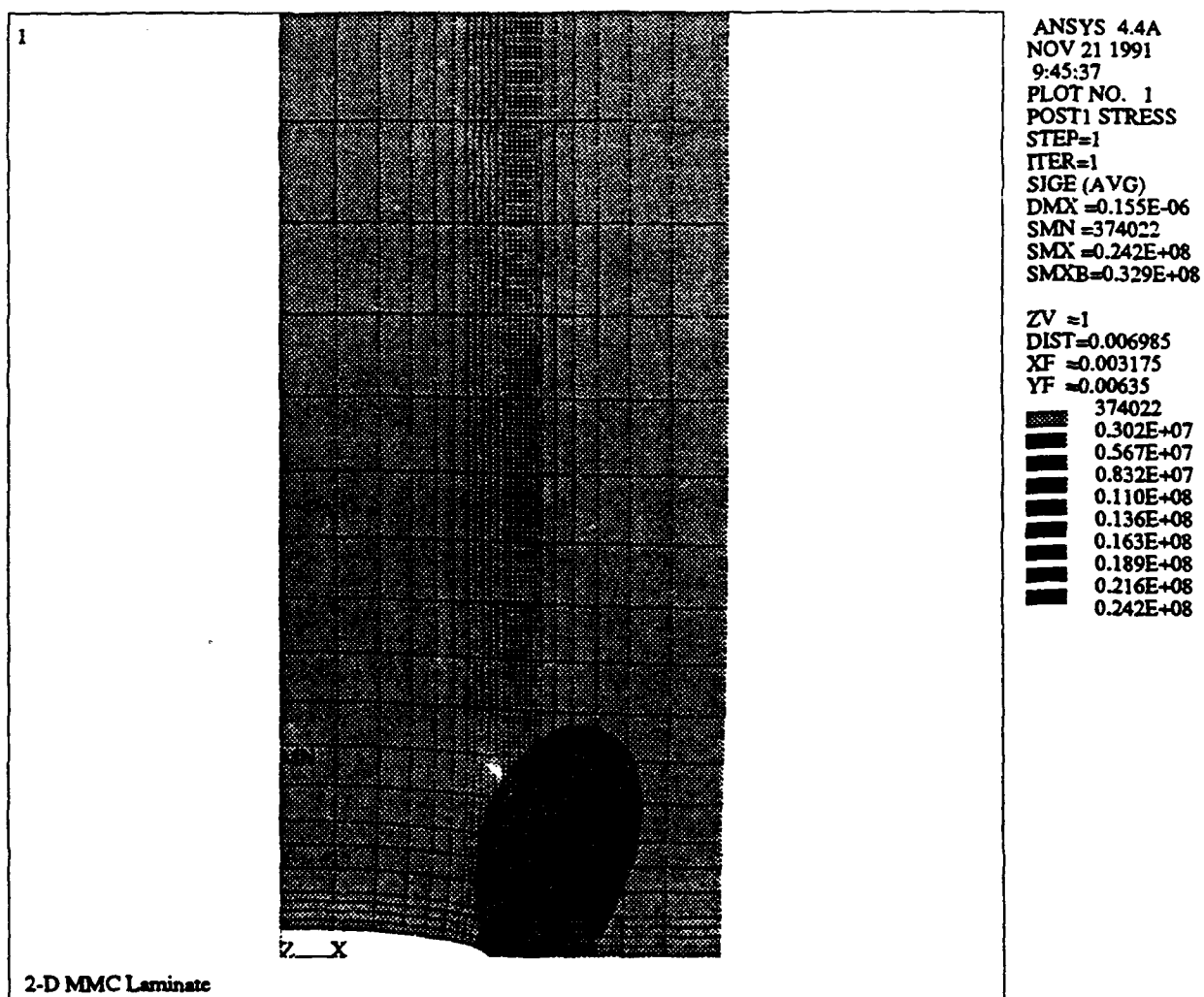


Figure 3.16. Effective stress contour plot in 456 element macroscopic model. The plate is modeled using quarter symmetry, the crack tip is located in the lower left corner.

fail according to equations 1.22 and 1.23 respectively as was described in Chapter 1. Since fiber pull-out and matrix plasticity may precede failure, the normal stress ratio and Von Mises yield criteria will be used to predict fiber debonding and matrix yielding respectively. The normal stress ratio in this case is equal to the transverse stress in the composite divided by σ_i , the tensile strength of the interface. Thus when the normal stress ratio exceeds 1.0 then interfacial failure will occur. Experimental results [48] indicate that fiber debonding occurs at transverse stresses as low as 138 MPa, well below the level required for matrix yielding and fiber failure. Thus the global model took into consideration material nonlinearities, but the solution did not reach the required stress state for plastic deformation.

As was described in detail in Chapter 2, the boundary conditions for the micro-model were extracted from the solution to the global model. The critical external load required to initiation fiber-matrix debonding was reached when $\sigma_x = 138$ MPa. Note from Table 2.2 that this is well below the stress level necessary to induce yielding. The induced displacements parallel (UX) and perpendicular (UY) to the direction of the crack were then plotted and fit with the best curve as shown in Figs 3.17 and 3.18. The four curves (A, B, C and D) represent the nodes of the macro-model as was depicted in Fig. 2.7. For the displacement along the crack tip direction, the fitted curves are given in equations 3.1 and 3.2 for curves C and D respectively.

$$y = -0.506 - 1.046 \times 10^{-4} \tau - 1.804 \times 10^{-7} \tau^2 \quad R^2 = 0.972 \quad (3.1)$$

$$y = -0.449 - 1.342 \times 10^{-4} \tau - 1.627 \times 10^{-7} \tau^2 \quad R^2 = 0.995 \quad (3.2)$$

For curves A and B, the R^2 correlation was less than 0.92, therefore visual interpolation was used to obtain the necessary points. For the displacements normal to the crack tip

direction, the fitted curves are given in equations 3.3-3.6 for curves A-D respectively.

$$y = 1.091 \times 10^{-3} - 5.144 \times 10^{-3} r - 2.435 \times 10^{-5} r^2 - 4.987 \times 10^{-8} r^3 \quad R^2 = 0.999 \quad (3.3)$$

$$y = 0.172 - 1.252 \times 10^{-3} r - 3.690 \times 10^{-6} r^2 - 6.318 \times 10^{-9} r^3 - 3.506 \times 10^{-11} r^4 \quad R^2 = 0.999 \quad (3.4)$$

$$y = 0.253 - 8.688 \times 10^{-4} r - 1.269 \times 10^{-6} r^2 \quad R^2 = 0.998 \quad (3.5)$$

$$y = 0.318 - 7.389 \times 10^{-4} r - 7.572 \times 10^{-7} r^2 \quad R^2 = 0.999 \quad (3.6)$$

Micro-Mechanics Analysis

The fiber, matrix and interphase regions are modeled as distinct materials on the local level. Boundary conditions were extracted from elements of the global model, as was described in the previous section, whose transverse stresses, σ_x , exceed the stress required to initiate fiber debonding. The height and sides of the local model are each 380 μm . Three different values of σ_i were used under identical boundary conditions. Figure 3.18 shows the deformed mesh when $\sigma_i = 138 \text{ MPa}$. The outlined area indicates the plane of the crack. Note that complete fiber debonding occurred along all three fibers. When the strength of the interface was increased to that of the fiber, extremely high stresses were developed within the fibers. This case does not merit additional discussion. As an intermediate value, σ_i was set equal to the strength of the matrix, and load is effectively transferred to the fibers. Figure 3.20 shows the stress contours when

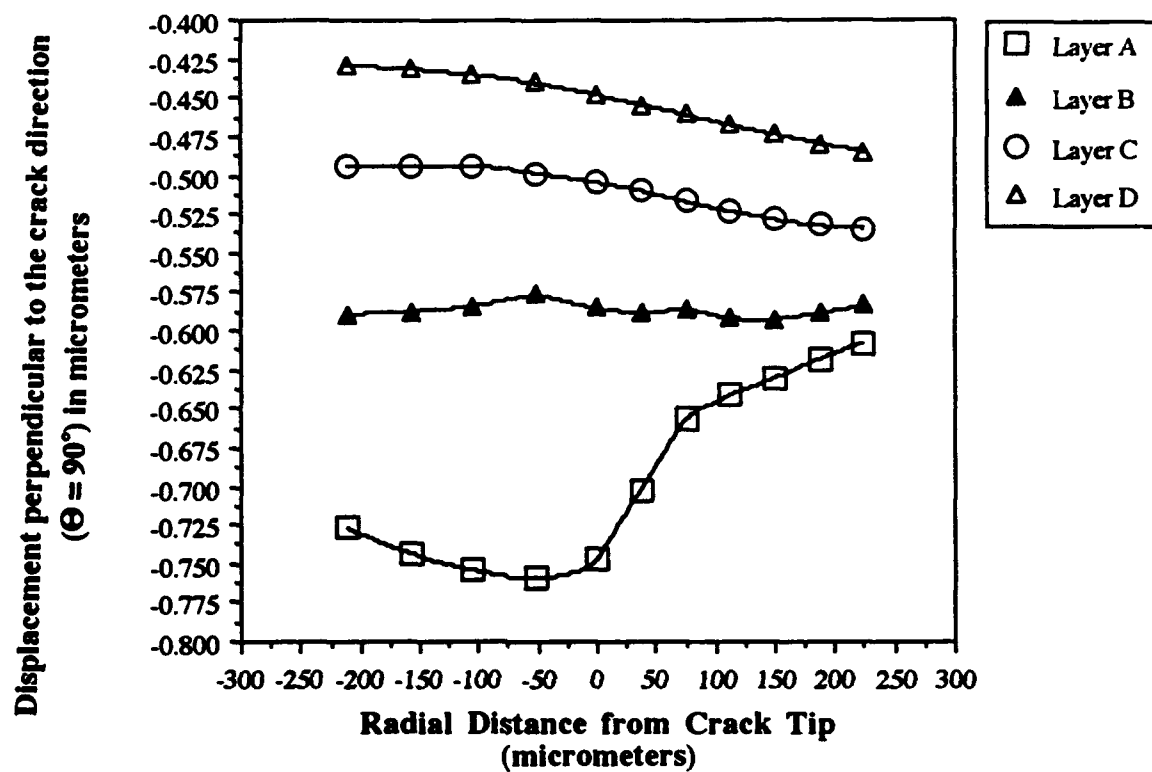


Figure 3.17. Displacements obtained from the solution of the global model. The data are interpolated using polynomial fits on layers D and C, while visual interpolation is used on layers B and A (refer to Fig. 2.7).

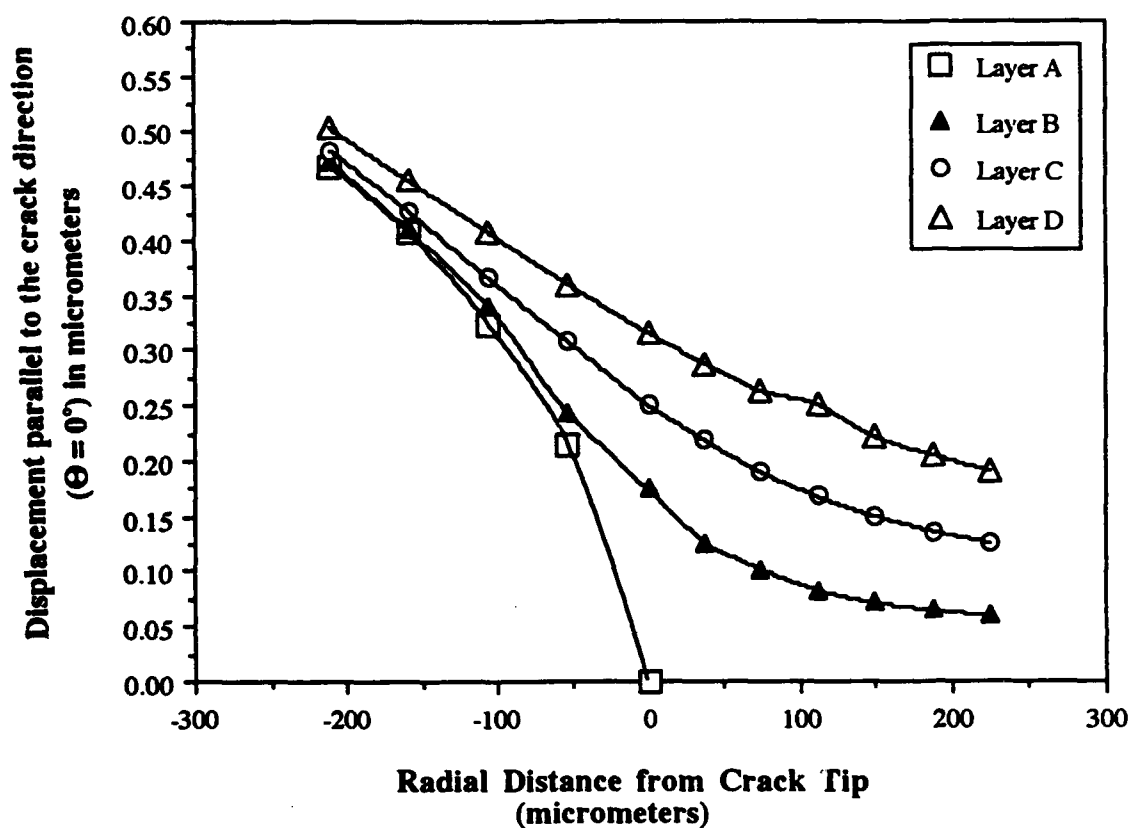


Figure 3.18. Displacements obtained from the solution of the global model. The data are interpolated using polynomial fits on all layers (refer to Fig. 2.7).

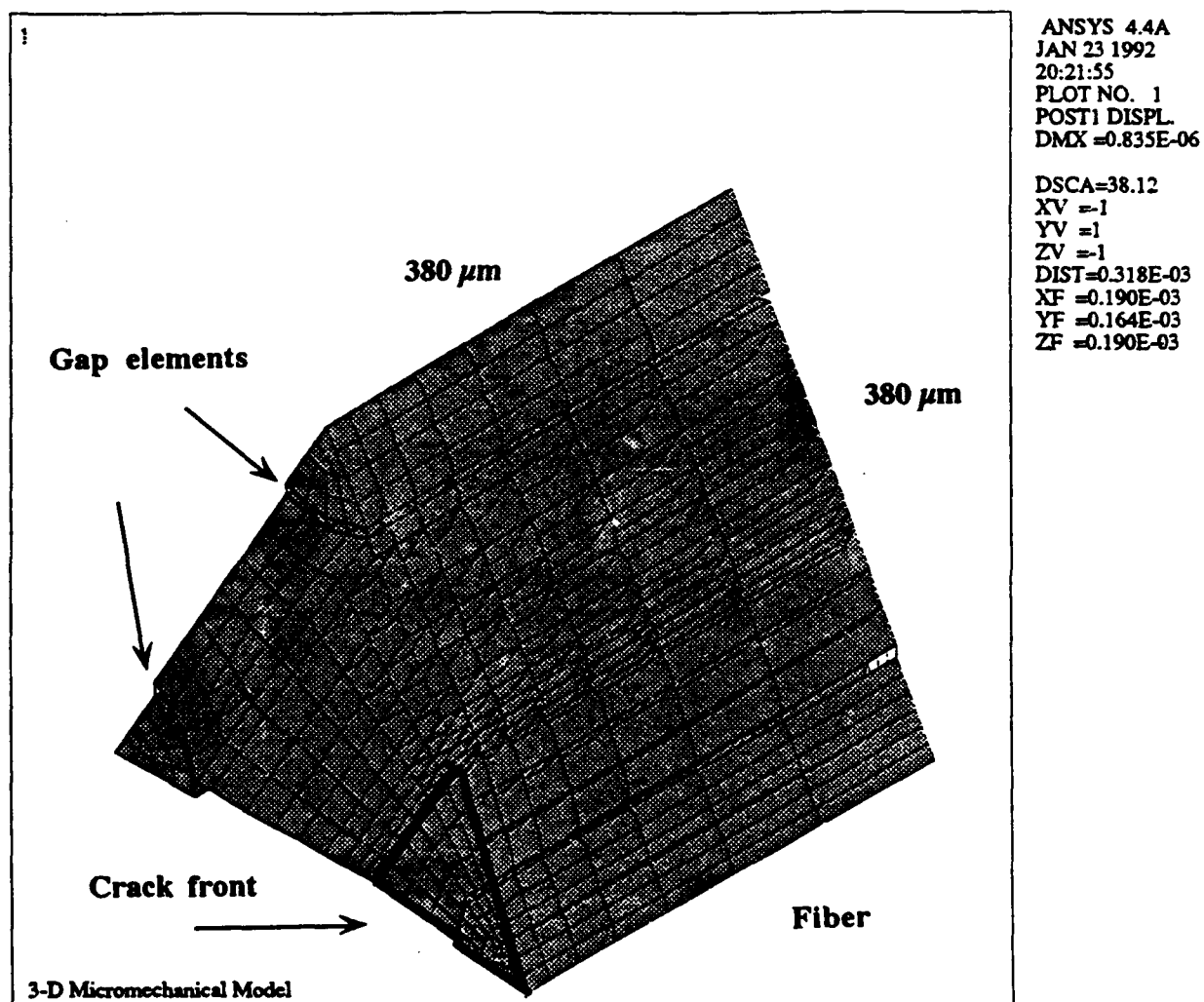


Figure 3.19. Deformed finite element mesh showing fiber debonding in SCS-6/Ti-15-3. Crack plane is outlined as shown.

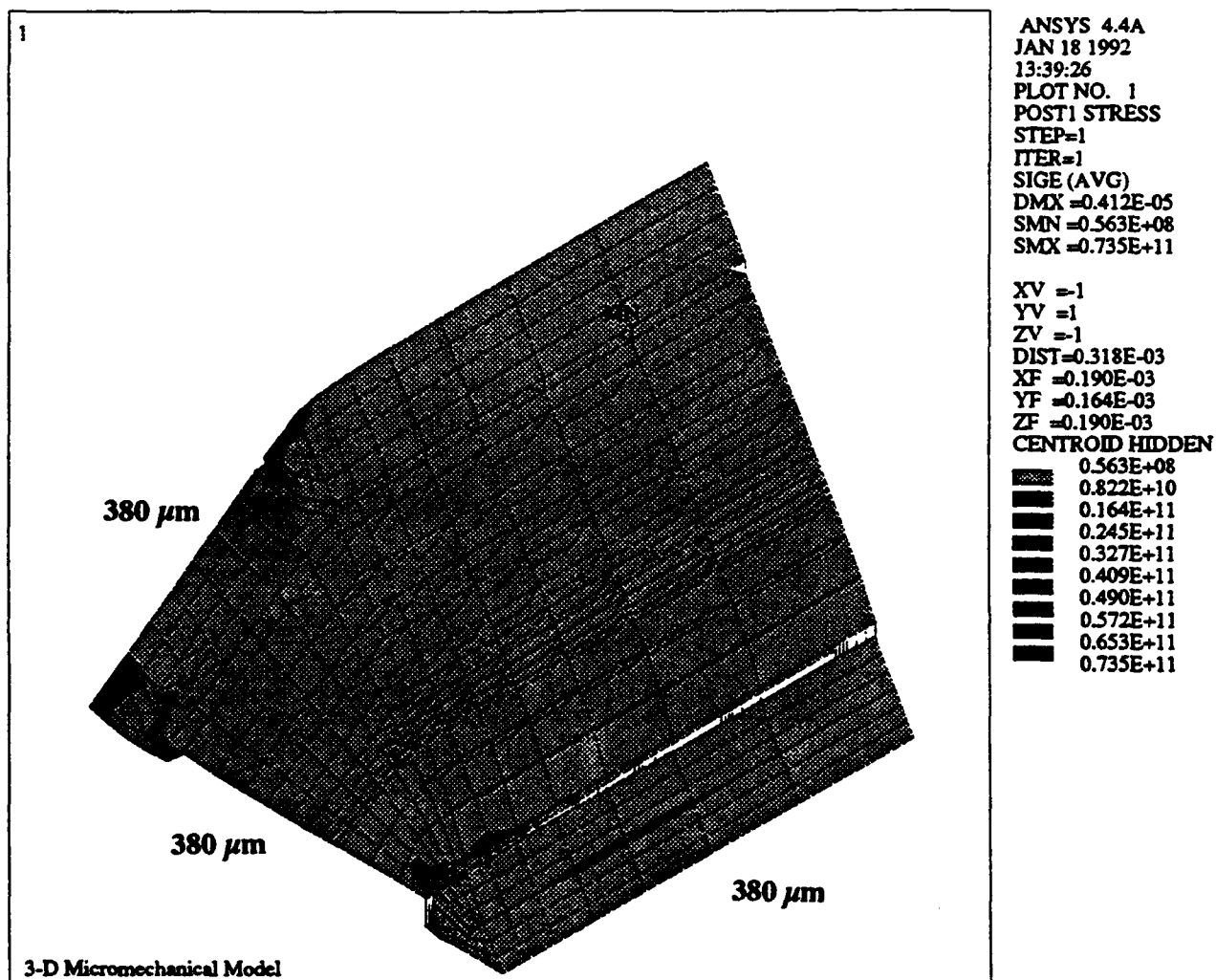


Figure 3.20. Effective stress contour in SCS-6/Ti-15-3 when $\sigma_i = 934$ MPa. Note that the stresses are concentrated within the fiber due to effective load transfer.

$\sigma_i = \sigma_m$. In this case the maximum stress within the fiber far exceeds its ultimate strength, indicating instantaneous fracture of the fibers under the assumed nature of the interface.

When relatively low loads (still well within the elastic limit) are developed about the crack tip in the global composite, substantial damage occurs on a microscopic scale. As was observed in monolithic steel and aluminum, the trend of stress decaying away from the crack tip is maintained as is shown in Fig. 3.21. When the signature of the stress field in the matrix near the crack tip is compared to the signature in monolithic metals, similarities are found. Note that at a finite distance from the crack tip, the stress increases then decreases once more.

By taking a closer look at the effective stresses near the interface region, it is possible to document the mechanics of load transfer. Figure 3.22 shows the orientation of a sectioned surface of the micro-model, including the three fibers labeled A, B and C. Figures 3.23, 3.24 and 3.25 exhibit how load is transferred from the matrix to the fibers using the right hand definite orientation described above. These three figures represent different degrees of interfacial bonding: 138 MPa, 534 MPa and 934 MPa. The load transfer ratio is defined in equation 3.7.

$$\text{Load transfer ratio} = \frac{\sigma_{\text{fiber}}}{\sigma_{\text{matrix}}} \quad (3.7)$$

From these plots, it is evident that on the average, the broken fiber does not transfer load as effectively as does the undamaged fibers. Also note that load transfer is not uniform and that it depends upon the angular orientation and distance from the crack front. In general, the interface regions on the plane of the crack front transfer more load than does the plane furthest from the crack front.

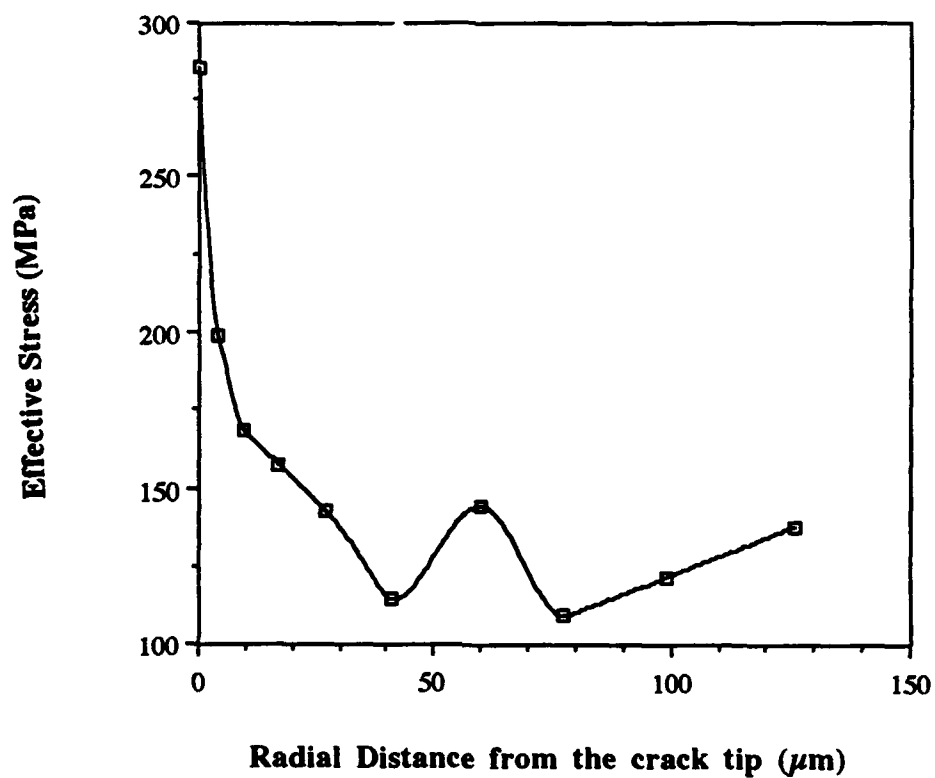


Figure 3.21. Plot of the effective stress against the radial distance from the crack tip in the normal direction to the crack front.

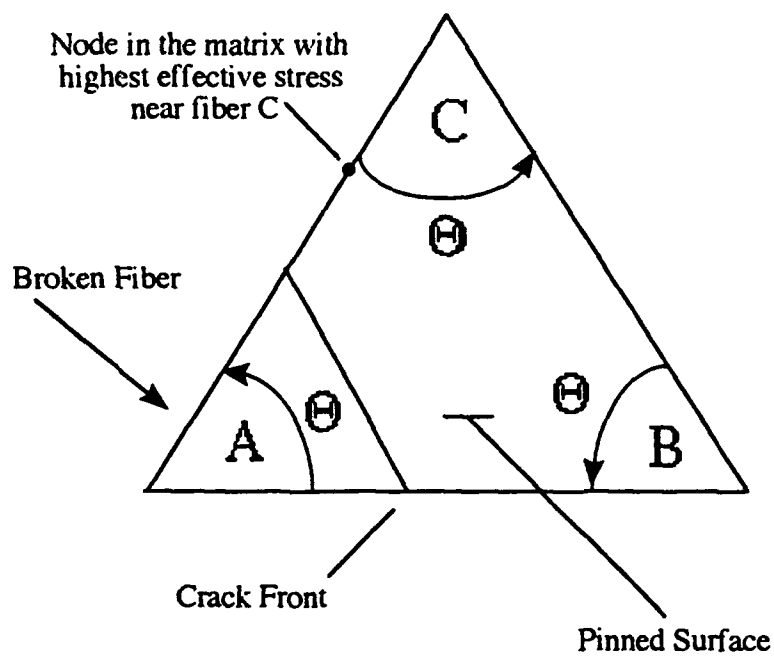


Figure 3.22. Schematic cross section of micro-model showing right hand definite angular orientation. Fiber A corresponds to the broken fiber, while fibers B and C remain unbroken.

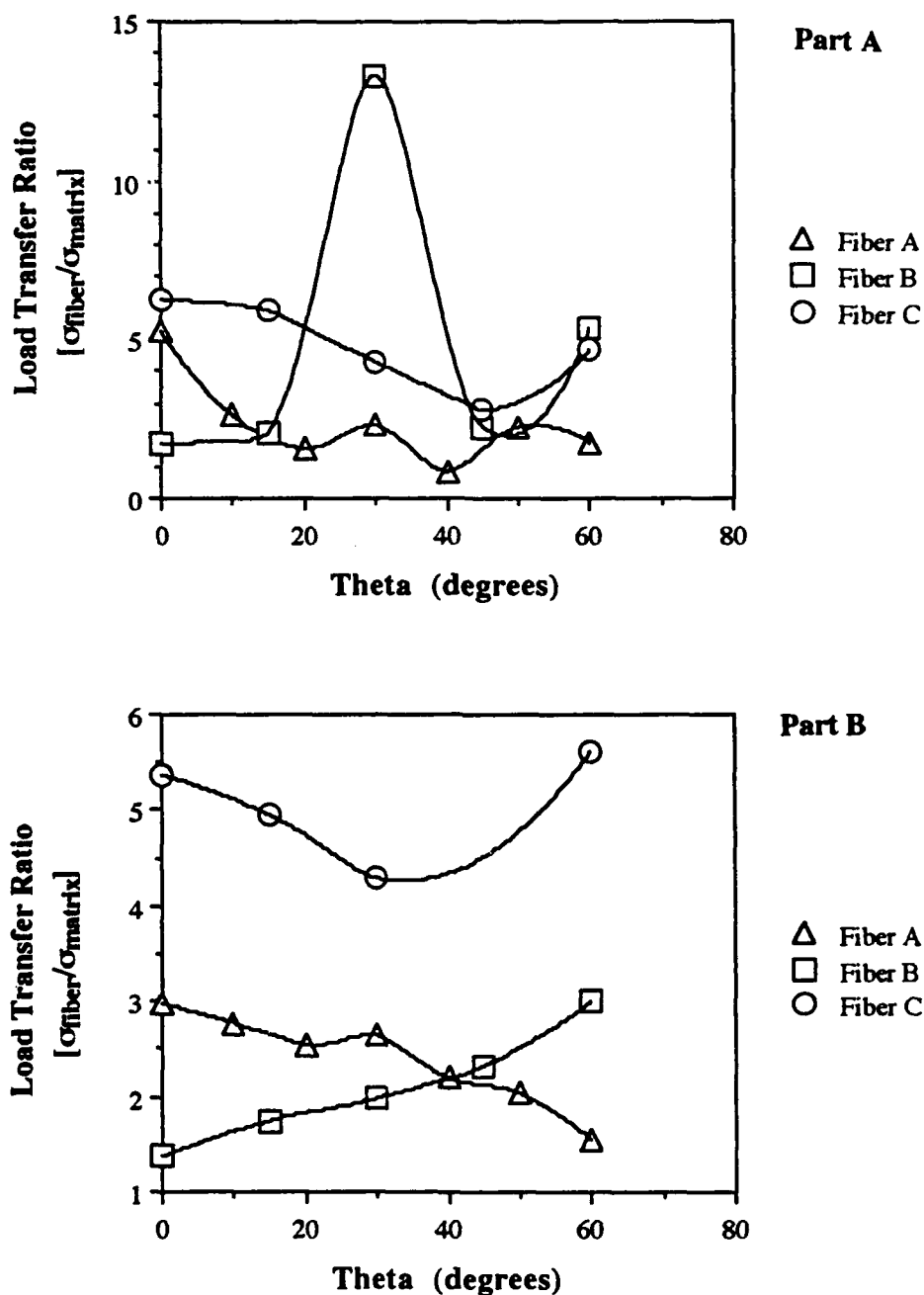


Figure 3.23. Part A shows effective load transfer in fibers A, B and C as a function of angular orientation on the crack plane. Part B shows effective load transfer on the plane furthest from the crack plane. The interface strength is 934 MPa.

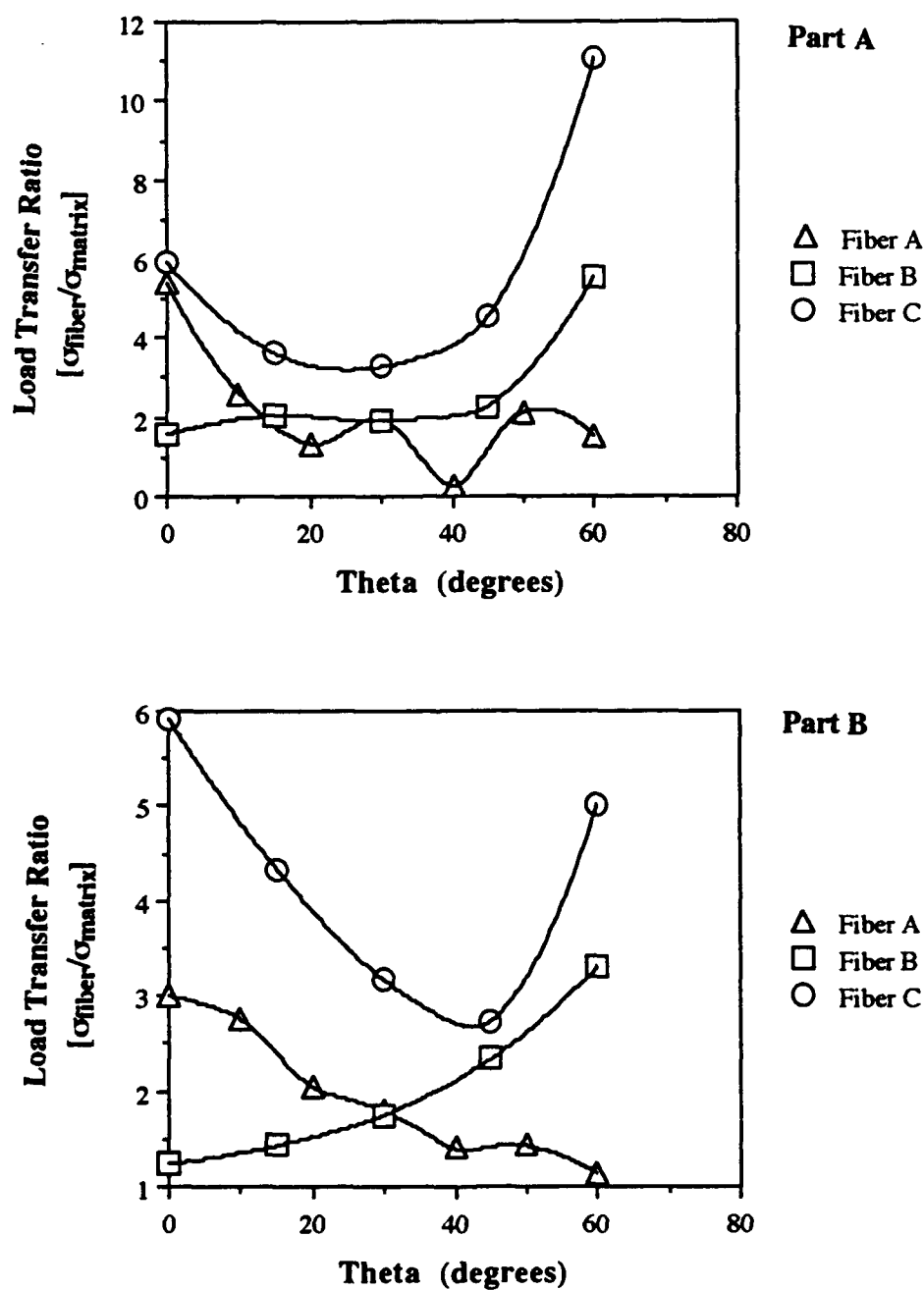


Figure 3.24. Part A shows effective load transfer in fibers A, B and C as a function of angular orientation on the crack plane. Part B shows effective load transfer on the plane furthest from the crack plane. The interface strength is 534 MPa.

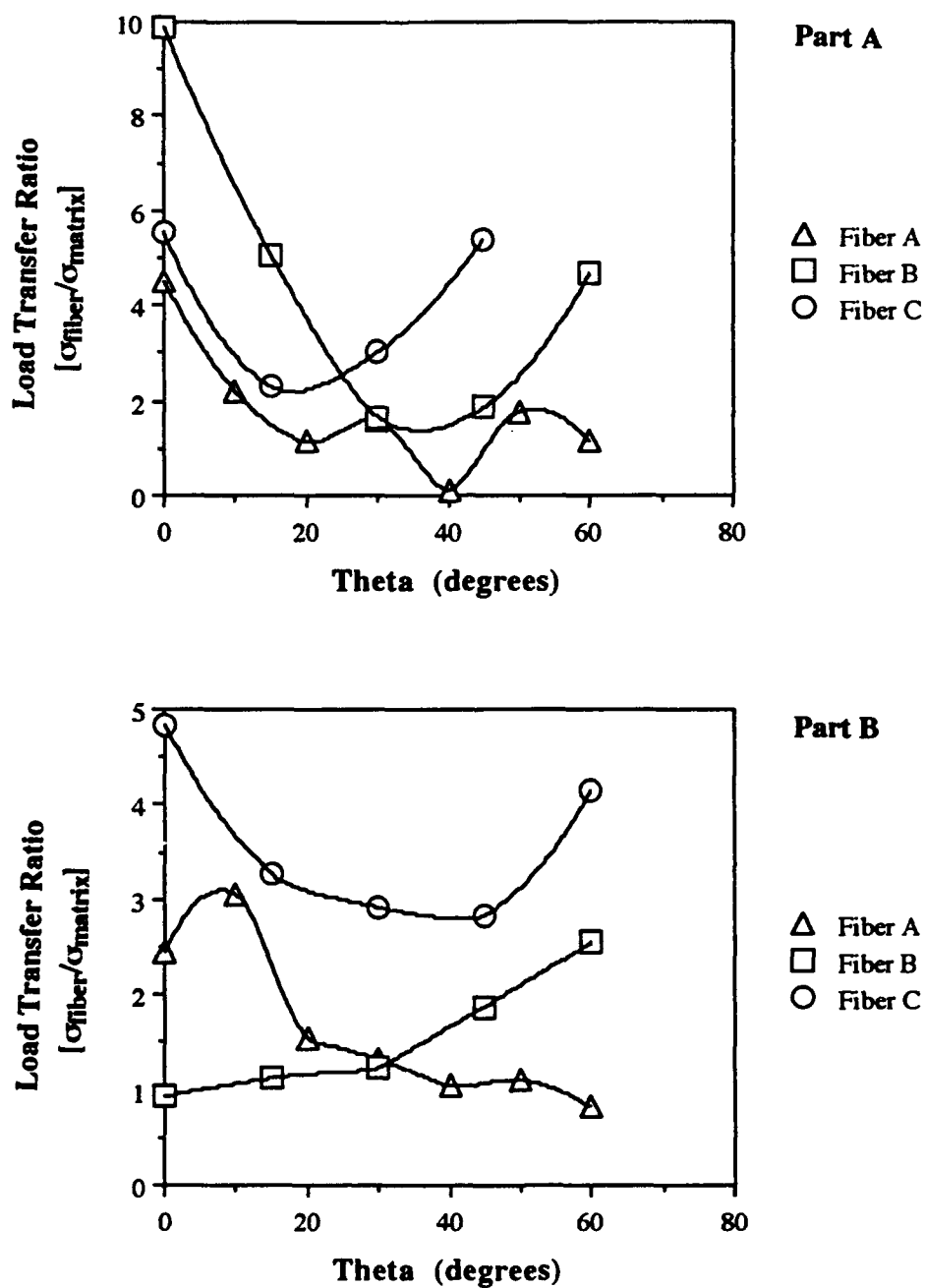


Figure 3.24. Part A shows effective load transfer in fibers A, B and C as a function of angular orientation on the crack plane. Part B shows effective load transfer on the plane furthest from the crack plane. The interface strength is 138 MPa.

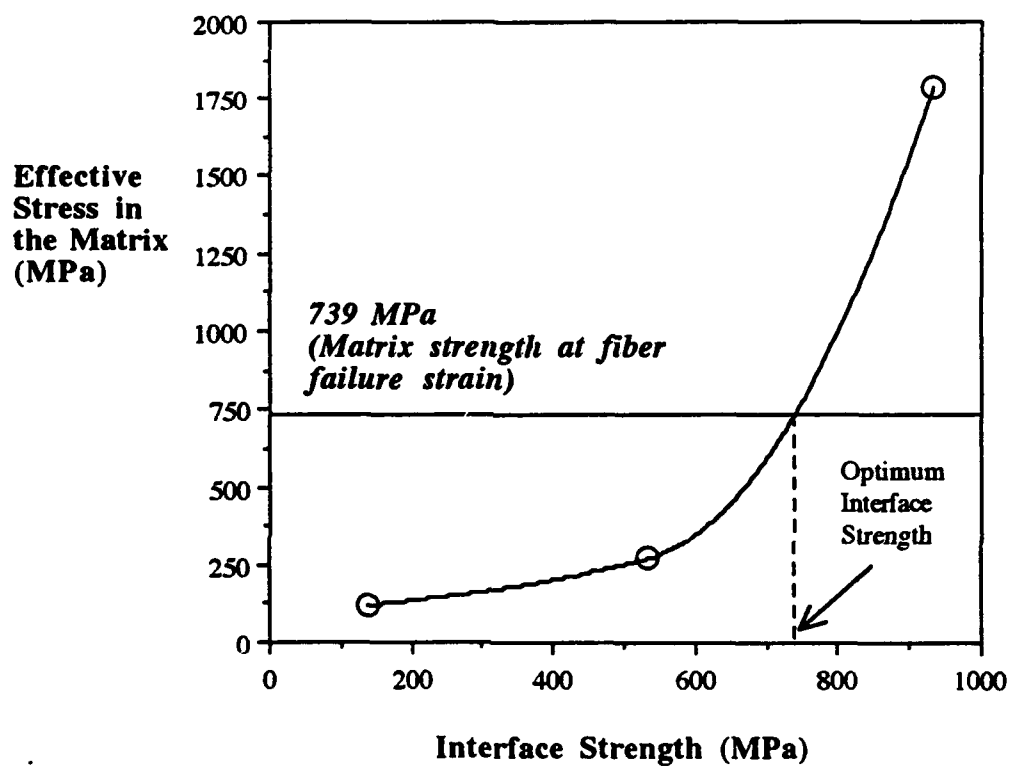


Figure 3.26. Optimization of the interface strength considering the stress in the matrix near the fiber-matrix interface ($E_i = 92.39$ GPa). The optimum value of the interface strength, $(\sigma_i)_{opt}$, may be obtained by reading the interface strength at the intercept of the two curves.

An estimate of the optimum interface strength, $(\sigma_i)_{opt}$, can be made by picking a single point in the matrix near the interface. The point chosen corresponds to the node at which the greatest effective stress is observed. Figure 3.26 shows that as the degree of interfacial bonding is increased beyond 730 MPa, the stress in the matrix exceeds 739 MPa, the stress in the matrix at the fracture strain of the SCS-6 fibers (0.8%). Therefore, when fabricating SCS-6/Ti-15-3 composites, it would be advantageous to increase the degree of interfacial bonding to 730 MPa. Keep in mind that this analysis uses an assumed value of the interface stiffness equal to that of the matrix stiffness.

CHAPTER 4

SUMMARY AND CONCLUSIONS

A series of materials have been evaluated numerically for their fracture behavior and response to applied loads. Monolithic HY-130 steel, HY-140 steel, 5083-O aluminum and 7075 aluminum have been studied using *ARLPAPST*, a nonlinear finite element package. In the case of HY-130 steel, 7075 aluminum and 5083-O aluminum, the strain energy distribution allows estimates of the crack initiation loads and the failure load to be made. The effect of crack tip plasticity and crack tip unloading on the *J*-Integral have been established. Values of the *J*-Integral were examined for a range of crack to width ratios ($0.533 \leq a/W \leq 0.884$) leading from small scale to extensive plasticity. When the loads were increased above a critical load (which is attributed to crack initiation), values of the *J*-Integral deviated from the averaged value across the ligament of the specimens, up to 13%.

The damage mechanics in the composite were studied using a local-global analysis. The boundary conditions for the three-dimensional micro-model were extracted from the two-dimensional macro-model through an innovative concept of coordinate rotation and interpolation. The results of the micro-mechanical modeling are valid when considering only the non-dimensionalized quantities and not the absolute numbers. The convergence test for the micro-model still needs to be performed. Within this context, extensive deformation and interfacial debonding were found near the crack tip of the composite even under the application of relatively low loads. These numerical predictions confirmed the published experimental observations that SCS-6/Ti-15-3

delaminates readily under loading. Extensive fiber debonding was observed when the interfacial strength was set to 138 MPa. Loads were more effectively transferred when the interface strength was increased above 138 MPa. Thus the optimum strength of the interface under the assumed conditions of the model is between 534 and 934 MPa. The signature of the effective stresses in the micro-mechanical model of the composite signifies the crack propagation direction as in the case of matrix materials.

CHAPTER 5

RECOMMENDATIONS FOR FUTURE RESEARCH

The recommendations for future work in the area of local-global finite element analysis will be itemized below:

- An iterative load stepping solution procedure is needed to determine the exact point of fiber failure and/or fiber matrix debonding.
- More values of the interface tensile strength, shear strength and stiffness need to be analyzed to optimize the point at which delamination is favored over fiber fracture.
- The micromechanical model is designed to easily accept different crack lengths. The effect of crack length on delamination and fiber fracture should be studied.
- The case of crack bridging should be studied by simply varying the boundary conditions of the micro-model.

REFERENCES

1. J.G. Bakuckas, C.W. Lau, and J. Awerbuch, "Damage Analysis of Notched Unidirectional Metal Matrix Composites"; pp. 43-55 in Proceedings of the Thirteenth International Symposium for Testing and Failure Analysis, ISTFA/87, Los Angeles, California, 1987.
2. Mahulikar, D.S., Y.H. Park and H.L. Marcus, "Mixed Mode Crack Propagation in Continuous Fiber Metal Matrix Composites"; pp. 385-395 in Mixed Mode Crack Propagation: Proceedings of First USA-Greece Symposium, Edited by G.C. Sih and P.S. Theocaris, 1981.
3. J.G. Goree and R.S. Gross, "Analysis of A Unidirectional Composite Containing Broken Fibers and Matrix Damage," *Engineering Fracture Mechanics*, 13, 563-578 (1979).
4. Z. Hashin and B. Rosen, "The Elastic Moduli of Fiber-Reinforced Materials," *Journal of Applied Mechanics*, 223-232 (1964).
5. R. Hill, "Continuum Micro-mechanics of Elastoplastic Polycrystals," *Journal of the Mechanics and Physics of Solids*, 13, 89-101 (1965).
6. W.S. Johnson, C.A. Bigelow and Y.A. Bahei-El-Din, " Experimental and Analytical Investigation of the Fracture Processes of Boron/Aluminum Laminates Containing Notches," NASA TP-2187 (1983).
7. M.S. Madhukar, J. Awerbuch, A.C.W. Lau, and E.S. Reddy, "A Nonlinear Lumped Fiber Model for the Analysis of Fracture Behavior of Notched Unidirectional Metal-Matrix Composites," *Engineering Fracture Mechanics*, 32 [1] 43-64 (1989).
8. R.A. Schapery, "Mechanical Characterization and Analysis of Inelastic Composite Laminates with Growing Damage"; pp. 1-9 in Mechanics of Composite Materials and Structures: Proceedings of the Third Joint ASCE/ASME Mechanics Conference University of California, San Diego, (1991).
9. V.M. Karbhari and D.J. Wilkings, "A Theoretical Model for Fiber Debonding Incorporating both Interfacial Shear and Frictional Stresses," *Scripta Metallurgica et Materialia*, 24, 1197-1202 (1990).
10. T.W. Clyne and M.C. Watson, "Interfacial Mechanics in Fibre-Reinforced Metals," *Composites Science and Technology*, 42, 25-55 (1991).
11. P.G. Charalambides and A.G. Evans, "Debonding Properties of Residually Stressed Brittle-Matrix Composites," *Journal of the American Ceramic Society*, 72 [5] 46-753 (1989).

12. R.R. Reynolds, K. Kokini and G. Chen, "The Mechanics of the Interface Crack Using the Finite Element Method," *Journal of Engineering Materials and Technology*, **12**, 38-43 (1990).
13. M.D. Thouless, O Sbaizero, L.S. Sigl and A.G. Evans, "Effect of Interface Mechanical Properties on Pullout in a SiC-Fiber-Reinforced Lithium Aluminum Silicate Glass-Ceramic," *Journal of the American Ceramic Society*, **72** [4] 525-532 (1989).
14. V. Gupta and A. Argon, "Crack Deflection at an Interface Between two Orthotropic Media," In press: *Journal of Applied Mechanics*.
15. C.A. Bigelow and R.A. Naik, "A Macro-micromechanics Analysis of a Notched Metal Matrix Composite," NASA TM-102728 (1990).
16. J. Renard, "Modelling of a Damaged Composite Specimen by a Micro-Macro Numerical Simulation"; pp. 57-62 in *Composite Material Technology 1990*, Edited by D. Hui and T.J. Kozik, 1990.
17. J.F. Wu, M.S. Shephard, G.J. Dvorak and Y.A. Bahei-El-Din, "A Material Model for the Finite Element Analysis of Metal Matrix Composites," *Composites Science and Technology*, **35**, 347-366 (1989).
18. E. Orowan, *Fatigue and Fracture of Metals*, MIT Press, Cambridge, MA, 1950.
19. S.H. Goods and L.M. Brown, "The Nucleation of Cavities by Plastic Deformation," *Acta Metallurgica*, **27**, 1-15 (1979).
20. C. Lee, "Spread of Plastic Deformation in Notched and Cracked Plates" Ph.D dissertation, University of South Carolina, 1987.
21. J.R. Rice, "A Path Independent Integral and the Approximate Analysis of Strain Concentration by Notches and Cracks," *Journal of Applied Mechanics*, **35**, 379-386 (1968).
22. J.A. Begley and J.D. Landes, "The J-Integral as a Fracture Criterion"; pp. 1-20 in *Fracture Toughness, Proceedings of the 1971 National Symposium on Fracture Mechanics, Part II*, ASTM STP 514, American Society for Testing and Materials, 1972.
23. J.W. Hutchinson, "Fundamentals of the Phenomenological Theory of Non-linear Fracture Mechanics," *ASME Journal of Applied Mechanics*, **50**, 1042-1051.
24. E.P. Sorensen, "A Numerical Investigation of Stable Crack Growth Under Small Scale Yielding Conditions"; pp. 151-174 in *Elastic-Plastic Fracture*, ASTM STP 668, Edited by J.D. Landes, J.A. Begley, and G.A. Clarke, American Society for Testing and Materials, 1979.

25. R.H Dean and J.W. Hutchinson, "Quasi-static Crack Growth in Small-Scale yielding"; pp. 383-405 in *Fracture Mechanics: Twelfth Conference, ASTM STP 700*, Edited by J.B. Wheeler, H.M. Hoersch and H. Mahy, American Society for Testing and Materials, 1980.
26. P.S. Lam and R.M. McMeeking, "Analysis of Steady Quasistatic Crack Growth in Plane Strain Tension in Elastic-Plastic Materials with Non-isotropic Hardening," *Journal of the Mechanics and Physics of Solids*, **32**, 395-414 (1984).
27. W. Brocks and H. Yuan, "Numerical Investigation on the Significance of J for Large Stable Crack Growth," *Engineering Fracture Mechanics*, **32** [3] 459-468 (1989).
28. S. Jun, L. Zhong-Hua, D. Zeng-Jie and T. Ming-Jing, "Crack-Tip Constraint and J -Controlling Stable Growth of Crack in Plane Stress Case," *Engineering Fracture Mechanics*, **39** [6] 1045-1049 (1991).
29. F.A. McClintock, "Plasticity Aspects of Fracture"; pp. 47-225 in *Fracture: An Advanced Treatise*, volume 3, Academic Press, New York, 1971.
30. J.W. Hutchinson, "Singular Behaviour at the End of a Tensile Crack in a Hardening Material," *Journal of the Mechanics and Physics of Solids*, **16**, 13-31 (1968).
31. J.R. Rice and G.F. Rosengren, "Plane Strain Deformation Near a Crack Tip in a Power-Law Hardening Material," *Journal of the Mechanics and Physics of Solids*, **16**, 1-12 (1968).
32. M.L. Vanderglas, "Experiences Using Three-Dimensional Finite Element Analysis for Leak-Before-Break Assessment," *International Journal of Pressure Vessels & Piping*, **43**, 241-253 (1990).
33. H.W. Liu, "On the Fundamental Basis of Fracture Mechanics," *Engineering Fracture Mechanics*, **17** [5] 425-438 (1983).
34. R.M. McMeeking, and D.M. Parks, "On Criteria for J Dominance of Crack Tip Fields in Large-Scale Yielding"; pp. 175-194 in *Elastic-Plastic Fracture, ASTM STP 668*, Edited by J.D. Landes, J.A. Begley, and G.A. Clarke, American Society for Testing and Materials, 1979.
35. R.M. McMeeking, "Finite Deformation Analysis of Crack-Tip Opening in Elastic-Plastic Materials and Implications for Fracture," *Journal of the Mechanics and Physics of Solids*, **25**, 357-381 (1977).
36. C.F. Shih and M.D. German, "Requirement for a One Parameter Characterization of Crack Tip Fields by the HRR Singularity," *International Journal of Fracture*, **17**, 27-43 (1981).

37. A. Needleman and V. Tvergaard, "Crack Tip Stress and Deformation in a Solid with a Vertex on its Yield Surface"; pp. I-80-I-115 in *Elastic-Plastic Fracture: 2nd Symposium, Vol. I--Inelastic Crack Analysis*, ASTM STP 803, Edited by C.F. Shih and J.P. Gudas, American Society for Testing and Materials, 1983.
38. W. Schmitt and R. Kienzler, "The *J*-Integral Concept for Elastic-Plastic Material Behavior," *Engineering Fracture Mechanics*, **32** [3] 409-418 (1989).
39. G.C. Sih, "Surface Layer Energy and Strain Energy Density for a Blunted Crack or Notch"; pp. 85-102 in *Prospects of Fracture Mechanics*, Edited by G.C. Sih, H.C. van Elst and D. Braek, Noordhoff International Publishing, Leyden, 1974.
40. G.C. Sih, "A special theory of crack propagation: methods of analysis and solutions of crack problems"; pp. 21-45 in *Mechanics of Fracture I*, Edited by G.C. Sih, Noordhoff International Publishing, Leyden, 1973.
41. C.M. Friend, "Toughness in metal matrix composites," *Materials Science and Technology*, **5**, 1-7 (1989).
42. D.L. Davidson, "Fracture Toughness in Particulate Metal Matrix Composites"; in *Metal Matrix Composites: Mechanisms and Properties*, Edited by R.K. Everett and R.J. Arsenault, Academic Press, 1990.
43. A. Magata and I.W. Hall, "Crack propagation in α -Al₂O₃/Mg Metal Matrix Composites," *Journal of Material Science*, **24** [6] 1959-1966 (1989).
44. M. Taya and R.J. Arsenault, *Metal Matrix Composites: Thermomechanical Behavior*, 1st ed. Pergamon Press, New York, 1990.
45. M.A. Wright, D. Welch and J. Jollay, "The Fracture of Fibre-reinforced 6061 Aluminium Alloy," *Journal of Material Science*, **14**, 1218-1228 (1979).
46. J. Awerbuch and H.T. Hahn, "Crack-Tip Damage and Fracture Toughness of Boron/Aluminum Composites," *Journal of Composite Materials*, **13**, 82-107 (1979).
47. R.J. Arsenault, "Relationship Between Strengthening Mechanisms and Fracture Toughness of Discontinuous SiC/Al Composites," *Journal of Composite Technology Resources*, **10** [4] 140-145 (1988).
48. W.S. Johnson, S.J. Lubowinski and A.L. Highsmith, "Mechanical Characterization of Unnotched SCS₆/Ti-15-3 Metal Matrix Composites at Room Temperature"; pp. 193-218 in *Thermal and Mechanical Behavior of Metal Matrix and Ceramic Matrix Composites*, ASTM STP 1080, Edited by J.M. Kennedy, H.H. Moeller, and W.S. Johnson, American Society for Testing and Materials, 1990.

49. M.K. Aghajanian, N.H. MacMillan, C.R. Kennedy, S.J. Laszczak and R. Roy, "Properties and Microstructure of Lanxide® Al₂O₃-Al Ceramic Composite Materials," *Journal of Material Science*, **24**, 658-670 (1989).
50. V. Gupta, A.S. Argon, D.M. Parks and J.A. Cornie, "Measurement of Interface Strength by a Laser Spallation Technique," In press: *Journal of the Mechanics and Physics of Solids*.
51. Z. Hashin, "Analysis of Composite Materials--A Survey," *Journal of Applied Mechanics*, **50**, 481-505 (1983).
52. G.J. Dvorak and Y.A. Bahei-El-Din, "Plasticity Analysis of Fibrous Composites," *Journal of Applied Mechanics*, **49**, 327-335 (1982).
53. G.J. Dvorak and Y.A. Bahei-El-Din, "Elastic-Plastic Behavior of Fibrous Composites," *Journal of the Mechanics and Physics of Solids*, **27**, 51-72 (1979).
54. J. Aboudi, "Elastoplasticity Theory for Composite Materials," *Solid Mechanics Archives*, **11**, 141-183 (1986).
55. J. Aboudi, "Micromechanical Prediction of Initial and Subsequent Yield Surfaces of Metal Matrix Composites," *International Journal of Plasticity*, **6**, 471-484 (1990).
56. W.S. Johnson and M.J. Birt, "Evaluation of Several Micromechanics Models for Discontinuously Reinforced Metal Matrix Composites," NASA TM-102719 (1990).
57. G. Laird and T.C. Kennedy, "Three-Dimensional Finite Element Analysis of a Crack in a Ceramic Composite"; pp. 233-241 in *Computers in Engineering 1990: Proceedings of the 1990 ASME International Computers in Engineering Conference and Exposition*, Boston, MA, 1990.
58. W.S. Kuo, N.J.J. Fang, A.P. Majidi, T.S. Chou, "Modeling and Characterization of Multi-Directionally Reinforced Ceramic Matrix Composites"; pp. 56:1-12 in NASA CP-10082 (1991).
59. B.P. Gupta, "Micromechanical Property Prediction for Flexible Matrix Composite Materials," *Journal of Engineering for Industry*, **109**, 29-33 (1987).
60. G.J. Dvorak and M.S. Madhava Rao, "Axisymmetric Plasticity Theory of Fibrous Composites," *International Journal of Engineering Science*, **14**, 361-373 (1976).
61. G.J. Dvorak and J.L. Teply, "Periodic Hexagonal Array Models for Plasticity Analysis of Composite Materials"; pp. 623-642 in *Plasticity Today: Modeling, Methods and Application*, Edited by A. Sawczuk and V. Bianchi, Elsevier Science Publishers, Amsterdam, 1985.

62. W.S. Johnson and C.A. Bigelow, "Elastic-Plastic Stress Concentrations Around Crack-like Notches in Continuous Fiber Reinforced Metal Matrix Composites"; pp. 261-275 in Text Methods for Design Allowables for Fibrous Composites: 2nd Volume, ASTM STP 1003, Edited by C.C. Chamis, American Society for Testing and Materials, 1989.
63. T.H. Lin, D. Salinas and Y.M. Ito, "Elastic-Plastic Analysis of Unidirectional Composites"; pp. 1-13 in Boron Reinforced Aluminum Systems volume 6, Edited by C.J. Hilado, Technomic Publishing Company, 1971.
64. N.J. Pagano and G.P. Tandon, "Thermo-elastic Model for Multidirectional Coated-fiber Composites: Traction Formulation," *Composites Science and Technology*, **38** [3] 247-269 (1990) .
65. R.L. Hinrichsen and A.N. Palazotto, "Nonlinear Finite Element Analysis of Thick Composite Plates Using Cubic Spline Functions," *AIAA Journal*, **24** [11] 1836-1842 (1986).
66. B.A. Lerch and M.E. Melis, "Experimental and Numerical Analysis of the Stress-Strain Behavior of a $[90^{\circ}/0^{\circ}]_2$ SiC/Ti Laminate"; pp. 39:1-11 in NASA CP-10082 (1991).
67. N.J. Pagano and G.P. Tandon, "Elastic Response of Multi-Directional Coated Fiber Composites," *Composites Science and Technology*, **31** [4] 273-293 (1988).
68. L.N. Gifford and P.D. Hilton, "Preliminary Documentation of PAPST--Nonlinear Fracture and Stress Analysis by Finite Elements," DTNSRDC Report 5602/30, 1981.
69. L.N. Gifford, "APES-Second Generation Two-Dimensional Fracture Mechanics and Stress Analysis by Finite Elements," DTNSRDC Report 4799, 1975.
70. L.N. Gifford, "APES-Finite Element Fracture Mechanics Analysis: Revised Documentation," DTNSRDC Report 79/023, 1979.
71. P.D. Hilton and L.N. Gifford, "Elastic-Plastic Finite Element Analysis of Two-Dimensional Crack Problems"; pp. 1256-1273 in Elastic-Plastic Fracture: 2nd Symposium, Vol. I--Inelastic Crack Analysis, ASTM STP 803, Edited by C.F. Shih and J.P. Gudas, American Society for Testing and Materials, 1983.
72. M.L. James, G.M. Smith and J.C. Wolford, Applied Numerical Methods for Digital Computation, 3d ed. Haper & Row, New York, 1985.
73. R.B. Bhagat, M.F. Amateau and M.L. Crocken, "Non-Linear Finite Element Analysis of Cracked A-517 Steel Compact Tensor Specimens"; pp. 285-297 in Proceedings of the 7th International Conference on Fracture, Edited by K. Salama, K. Ravi-Chandar, D.M.R. Taplin and P. Rama Rao, 1989.

74. Metals Handbook volume 2, Edited by H.E. Boyer and T.L. Gall, Metals Park, OH, American Society for Metals, 1985.
75. J.G. Kaufman, F.G. Nelson and R.H. Wygonik, "Large-Scale Fracture Toughness Tests of Thick 5083-O Plate and 5183 Welded Panels at Room Temperature, -260 and -320°F"; pp. 125-158 in Fatigue and Fracture Toughness--Cryogenic Behavior, ASTM STP 556, American Society for Testing and Materials, 1974.

APPENDIX A

J-INTEGRAL CUTTING PROGRAM

```
C   J-Integral cutting program (JCUT.FOR) created by Mike House on
C                                   20-SEP-1990 11:19:07.02
C
C >>>OBJECTIVE<<<      To cut the J-Integral values directly from the main
C                        PAPST output. Program can handle any number of
C                        increments.
C
C >>>COMMENTS<<<      Must change the input and output files to be accessed
C                        by program within the open statements.
C-----
C      CHARACTER*1 A(132)
C      CHARACTER B*10,LOADS*40
C      CHARACTER*11 JINT(15,50),CHECK
C      OPEN(UNIT=18,FILE='[mbh.monolith.HY-130.PAPST6]papst6.out',
C        .STATUS='OLD')
C      OPEN(UNIT=21,FILE='[mbh.monolith.HY-130.PAPST6]j130-3.OUT',
C        .STATUS='NEW')
C      REWIND 18
C      WRITE(*,10)
10    FORMAT(5X,'INPUT NUMBER OF PATHS CALCULATED FOR J-
      .INTEGRAL')
C      READ *, NJINT
C      WRITE(*,40)
40    FORMAT(5X,'INPUT NUMBER OF LOAD INCREMENTS')
C      READ *, NINC
C-----
C      CUT DATA FROM MAIN OUTPUT
C-----
C      DO 100 I=1,NINC
C        DO 200 J=1,NJINT
C          READ(18,5000) B,CHECK
3          FORMAT(T12,A10,T39,A11)
5000        IF(B.EQ.'J INTEGRAL') THEN
C            JINT(J,I)=CHECK
C            GO TO 200
C          ELSEIF(B.EQ.'INCREMENT ') THEN
C            DO 5003 JJ=1,NINC+1
C              READ(18,5001) LOADS
5001            FORMAT(T14,A40)
C              WRITE(21,5002) LOADS
```

```
5002             FORMAT(T10,A40)
5003             CONTINUE
              GO TO 3
          ELSE
              GO TO 3
          ENDIF
200             CONTINUE
100             CONTINUE
C-----
          DO 450 JCOL=1,NINC
              WRITE(21,110) JCOL
110             FORMAT(/T7,'VALUES OF THE J-INTEGRAL FOR INCREMENT
              .I3//T3,'PATH',T10,'J-INTEGRAL'/T3,'----',T10,'-----'/)
              DO 440 IROW=1,NJINT
                  WRITE(21,460) IROW,JINT(IROW,JCOL)
460                 FORMAT(T4,I2,T10,A11)
440                 CONTINUE
450             CONTINUE
              STOP
              END
```

APPENDIX B

POSTSCRIPT CONNECTIVITY PROGRAM

```
C          POSTSCRIPT Connectivity program
C          created by Mike House on 20-AUG-1991 19:52:11.02
C
C >>>OBJECTIVE<<<    To generate model meshes showing connectivity
C
C >>>VARIABLES<<<    NN = Number of nodes in the mesh
C                      NE = Number of elements in the model
C                      MAXSPW = Specimen width in inches
C
C >>>COMMENTS<<<    Necessary files includes the raw data file, all corner
C                      nodes and their connectivity (this is usually the data
C                      submitted to PAPST), a file containing the
C                      coordinates of the corner nodes, and the output file.
C-----
C          REAL*8 X(5000),Y(5000),MAXSPW,DEFX(5000,50),DEFY(5000,50)
C          CHARACTER*10 JUNK,JUNK3
C          CHARACTER*11 JUNK2
C          INTEGER C1(500),C2(500),C3(500),C4(500),MAT(500),DEFORM
C
C          READ(7,12) NN,NE,NM
12      FORMAT(3I5)
C          ISKIP = NM *2
C          DO 14 I=1,ISKIP
C              READ(7,15)JUNK
15      FORMAT(A10)
14      CONTINUE
C
C          MAXSPW = 0.000001
C          DO 1000 I=1,NN
C              READ(11,20) X(I),Y(I)
C              IF(X(I).GE.MAXSPW) MAXSPW=X(I)
20      FORMAT(T17,F9.7,11X,F9.7)
1000  CONTINUE
C          Code now calculates size of grid to place onto paper
C
C          IWIDTH = 432.0/MAXSPW
C
C          Postscript recognizes 72.0 dpi, therefore there are 72*8.5 columns
C          432.0 allows for 1.5" left margin and 1.0" right margin
C
```

```

WRITE(10,10) IWIDTH,IWIDTH
C
WRITE(6,16)
16  FORMAT(T5,'Is data in 2/corner mode or full mode? (1=2/corner)')
    READ(5,*) MODE
    IF(MODE.EQ.1) THEN
        DO 6000 J=1,2
            READ(7,18) C1(J),C2(J),C3(J),C4(J),MAT(J)
            WRITE(10,2) X(C1(J)),Y(C1(J)),X(C2(J)),Y(C2(J)),X(C3(J)),
        .Y(C3(J)),X(C4(J)),Y(C4(J)),X(C1(J)),Y(C1(J))
6000  CONTINUE
        DO 2000 J=3,NE
            READ(7,1020) C1(J),C2(J),C3(J),C4(J),MAT(J)
            WRITE(10,2) X(C1(J)),Y(C1(J)),X(C2(J)),Y(C2(J)),X(C3(J)),
        .Y(C3(J)),X(C4(J)),Y(C4(J)),X(C1(J)),Y(C1(J))
2000  CONTINUE
        ELSEIF(MODE.NE.1) THEN
            DO 19 J=1,NE
                READ(7,18) C1(J),C2(J),C3(J),C4(J),MAT(J)
                WRITE(10,2) X(C1(J)),Y(C1(J)),X(C2(J)),Y(C2(J)),X(C3(J)),
        .Y(C3(J)),X(C4(J)),Y(C4(J)),X(C1(J)),Y(C1(J))
19    CONTINUE
            ENDIF
            WRITE(10,5)
5    FORMAT(T2,' 0.6 setgray')
C
DO 46 J=1,NE
    IF(MAT(J).EQ.2) THEN
        WRITE(10,4) X(C1(J)),Y(C1(J)),X(C2(J)),Y(C2(J)),X(C3(J)),
        .Y(C3(J)),X(C4(J)),Y(C4(J)),X(C1(J)),Y(C1(J))
    ENDIF
46  CONTINUE
C
C  Now we want to read in displaced nodal values and add to X and Y
C
WRITE(6,4002)
4002 FORMAT(T5,'Print deformed mesh? (1=yes)')
    READ(5,*) DEFORM
    IF(DEFORM.EQ.1) THEN
        GOTO 9998
    ELSE
        GOTO 9999
    ENDIF
9998 WRITE(6,4003)
4003 FORMAT(T5,'How many converged solutions?')
    READ(5,*) INUM
    DO 6001 I1=1,NN
        DEFX(I1,1)=X(I1)
        DEFY(I1,1)=Y(I1)
6001 CONTINUE
C

```

```

DO 4300 K=1,INUM
4030     READ(15,4000) JUNK2
4000     FORMAT(T10,A11)
        IF(JUNK2.EQ.'NODE NUMBER') THEN
            READ(15,*)
            DO 4100 J=1,NN
                READ(15,4010) DX,DY
4010         FORMAT(T25,E11.8,T45,E11.8)
                DEFX(J,K)=X(J)+DX
                DEFY(J,K)=Y(J)+DY
4100         CONTINUE
            GOTO 4300
        ENDIF
        GOTO 4030
4300 CONTINUE
C
C Now develop format for datafile
C
4200 WRITE(6,4201)
4201 FORMAT(T5,'Overlay which converged solution?')
        READ(5,*) IC
        DO 4301 J=1,NE
            WRITE(10,2) DEFX(C1(J),IC),DEFY(C1(J),IC),DEFX(C2(J),IC),
                .DEFY(C2(J),IC),DEFX(C3(J),IC),DEFY(C3(J),IC),DEFX(C4(J),IC),
                .DEFY(C4(J),IC),DEFX(C1(J),IC),DEFY(C1(J),IC)
4301 CONTINUE
2      FORMAT(2X,F10.8,1X,F10.8,' moveto ',F10.8,1X,F10.8,' lineto ' /
        .1X,F10.8,1X,F10.8,' lineto ',F10.8,1X,F10.8,' lineto '/1X,F10.8,
        .1X,F10.8,' lineto stroke')
4      FORMAT(2X,F10.8,1X,F10.8,' moveto ',F10.8,1X,F10.8,' lineto ' /
        .1X,F10.8,1X,F10.8,' lineto ',F10.8,1X,F10.8,' lineto '/1X,F10.8,
        .1X,F10.8,' lineto fill')
C
C This is for all nodes given
C
18     FORMAT(T8,I3,T23,I3,T38,I3,T53,I3,T70,I1)
10     FORMAT(' %!' 103 320 translate'' 0 setlinewidth' /
        .T2,I4,1x,I4' scale')
C
C This is for only corner nodes given
C
1020   FORMAT(T8,I3,T13,I3,T18,I3,T23,I3,T70,I1)
9999   WRITE(10,3)
3       FORMAT(' showpage')
        STOP
        END

```

APPENDIX C

PROGRAM LISTING OF 2-D ORTHOTROPIC PROBLEM

```
/SHOW,X11
/PREP7
/title, 2-D MMC Laminate
CSYS,0          ! Define cartesian coordinates
KAN,0          ! Define static analysis
KAY,6,0        ! Small deflection option
ET,1,82,,,3,,2
R,THICKNESS,1.55E-3
K,1,0,0        ! Define keypoints 1-8
K,2,2.65e-3,0
K,3,3.175e-3,0
K,4,3.7e-3,0
K,5,6.35e-3,0
K,6,0,0.525e-3
K,7,2.65e-3,0.525e-3
K,8,3.175e-3,0.525e-3
K,9,3.7e-3,0.525e-3
K,10,6.35e-3,0.525e-3
K,11,0,1.525e-3
K,12,2.65e-3,1.525e-3
K,13,3.175e-3,1.525e-3
K,14,3.7e-3,1.525e-3
K,15,6.35e-3,1.525e-3
K,16,0,12.7e-3
K,17,2.65e-3,12.7e-3
K,18,3.175e-3,12.7e-3
K,19,3.7e-3,12.7e-3
K,20,6.35e-3,12.7e-3
/VIEW,1,1,1,1  ! Change perspective
L,2,1,3        ! List nodes as from,to,div,ratio
L,2,3,3
L,3,4,4
L,4,5,3
L,7,6,3
L,7,8,3
L,8,9,4
L,9,10,3
L,12,11,3
L,12,13,3
L,13,14,4
```

```

L,14,15,3
L,17,16,3
L,17,18,3
L,18,19,4
L,19,20,3
L,1,6,3
L,2,7,3
L,3,8,3
L,4,9,3
L,5,10,3
L,6,11,2
L,7,12,2
L,8,13,2
L,9,14,2
L,10,15,2
L,11,16,10,3
L,12,17,10,3
L,13,18,10,3
L,14,19,10,3
L,15,20,10,3
ELSIZE,,2
A,1,2,7,6
A,2,3,8,7
A,3,4,9,8
A,4,5,10,9
AMESH,1,4
ELSIZE,,2
A,6,7,12,11
A,7,8,13,12
A,8,9,14,13
A,9,10,15,14
AMESH,5,8
A,11,12,17,16
A,12,13,18,17
A,13,14,19,18
A,14,15,20,19
AMESH,9,12
ITER,1,1,1
KBC,0
MP,EX,1,122.7266E9
MP,EY,1,208.222E9
MP,NUXY,1,0.299
LSBC,22
LSBC,17
LSBC,27
LSBC,3
LSBC,4
KD,16,UY,2.4983954e-6,,1
KD,17,UY,2.4983954e-6,,1
KD,18,UY,2.4983954e-6,,1
KD,19,UY,2.4983954e-6,,1

```

! Up and down segments

!Default number of elem divisions

! MESH AREAS 5 TO 8

! DEFINES SYMMETRIC BC'S

KD,20,UY,2.4983954e-6,,1
SBCTRA ! TRANSFERS BC'S TO MESH
WAVE